water

MDPI

Article

Cd(II) and Pb(II) Adsorption Using a Composite Obtained from *Moringa oleifera* Lam. Cellulose Nanofibrils Impregnated with Iron Nanoparticles

Adriana Vázquez-Guerrero [1], Raúl Cortés-Martínez [2,*], Ruth Alfaro-Cuevas-Villanueva [3], Eric M. Rivera-Muñoz [4] and Rafael Huirache-Acuña [1,*]

1 División de Estudios de Posgrado, Facultad Ingeniería Química, Universidad Michoacana de San Nicolás de Hidalgo Edificio M, Ciudad Universitaria, C.P. 58030 Morelia, Mexico; adris.mokona@gmail.com
2 Facultad de Químico Farmacobiología, Universidad Michoacana de San Nicolás de Hidalgo, Tzintzuntzan 173, Colonia Matamoros, C.P. 58240 Morelia, Mexico
3 Instituto de Investigaciones en Ciencias de la Tierra, Universidad Michoacana de San Nicolás de Hidalgo, Edificio U5, Ciudad Universitaria, C.P. 58030 Morelia, Mexico; racv11@gmail.com
4 Centro de Física Aplicada y Tecnología Avanzada, Universidad Nacional Autónoma de México, Campus Juriquilla, C.P. 76230 Querétaro, Mexico; emrivera@fata.unam.mx
* Correspondence: raulcortesmtz@gmail.com (R.C.-M.); rafael_huirache@yahoo.it (R.H.-A.)

Abstract: This work informs on the green synthesis of a novel adsorbent and its adsorption capacity. The adsorbent was synthesized by the combination of iron nanoparticles and cellulose nanofibers (FeNPs/NFCs). Cellulose nanofibers (NFCs) were obtained from Moringa (*Moringa oleifera* Lam.) by a pulping Kraft process, acid hydrolysis, and ultrasonic methods. The adsorption method has advantages such as high heavy metal removal in water treatment. Therefore, cadmium (Cd) and lead (Pb) adsorption with FeNP/NFC from aqueous solutions in batch systems was investigated. The kinetic, isotherm, and thermodynamic parameters, as well as the adsorption capacities of FeNP/NFC in each system at different temperatures, were evaluated. The adsorption kinetic data were fitted to mathematical models, so the pseudo-second-order kinetic model described both Cd and Pb. The kinetic rate constant (K_2), was higher for Cd than for Pb, indicating that the metal adsorption was very fast. The adsorption isotherm data were best described by the Langmuir–Freundlich model for Pb multilayer adsorption. The Langmuir model described Cd monolayer sorption. However, experimental maximum adsorption capacities ($q_{e\,exp}$) for Cd (>12 mg/g) were lower than those for Pb (>80 mg/g). In conclusion, iron nanoparticles on the FeNP/NFC composite improved Cd and Pb selectivity during adsorption processes, indicating the process' spontaneous and exothermic nature.

Keywords: cadmium; lead; adsorption; cellulose nanofibrils; iron nanoparticles

Citation: Vázquez-Guerrero, A.; Cortés-Martínez, R.; Alfaro-Cuevas-Villanueva, R.; Rivera-Muñoz, E.M.; Huirache-Acuña, R. Cd(II) and Pb(II) Adsorption Using a Composite Obtained from *Moringa oleifera* Lam. Cellulose Nanofibrils Impregnated with Iron Nanoparticles. *Water* **2021**, *13*, 89. https://doi.org/10.3390/w13010089

Received: 26 November 2020
Accepted: 28 December 2020
Published: 3 January 2021

1. Introduction

Water pollution by heavy metals is one of the most severe environmental problems, with industrial processes being their main anthropogenic sources. Heavy metals can be distinguished from other pollutants because they are not biodegradable, and they can be bioaccumulated in different food chains. Furthermore, these metals have been linked to carcinogenic, embryotoxic, teratogenic, and mutagenic effects [1,2]. Consequently, the permissible limits for cadmium (Cd) and lead (Pb) in drinking water established in 2017 by the World Health Organization's (WHO) standards are 0.003 and 0.01 mg/L, respectively. The United States Environmental Protection Agency (USEPA) has set the maximum contaminant levels (MCLs) in drinking water at 0.015 mg/L for lead and 0.005 mg/L for cadmium [3–5]. Cadmium and lead are some of the heavy metals introduced as anthropogenic pollutants worldwide by various processes. Cadmium contamination may occur due to the manufacture of alloys, batteries, pigments, plastics, mining, and refining processes [6]. Cadmium causes severe damage to kidneys and bones. Its accumulation in

the human body leads to nausea, headaches, fatigue, salivation, diarrhea, muscular cramps, renal degradation, chronic pulmonary problems, skeletal deformity, low levels of iron in the blood, and breathlessness (dyspnea) [7,8].

On the other hand, common anthropogenic causes of lead contamination in groundwater are mining, smelting, fossil fuel combustion, solid waste incineration, batteries, paints, cables, ceramics, and glass manufacturing [9]. In children, overexposure to lead causes swelling of the optic nerve, ataxia, brain damage (encephalopathy), convulsions, seizures, and impaired consciousness. In adults, lead exposure causes high blood pressure, damage to the reproductive organs, fever, headaches, fatigue, vomiting, anorexia, abdominal pain, constipation, joint pain, incoordination, insomnia, irritability, and various symptoms related to the nervous systems [7].

Many techniques have been employed to reduce the adverse effects of cadmium and lead in water bodies, including chemical oxidation/reduction, chemical precipitation, electrochemical processes, ion exchange, membrane filtration, and others [10,11]. These processes can be difficult to operate, and they show low selectivity. However, among these methods, adsorption is flexible, low cost, and a high-efficiency technique [12]. Adsorption is a mass transfer process by which a substance is transferred from the liquid phase to the solid's surface by physical or chemical interactions.

Other studies have demonstrated the use of biomaterials as efficient, low-cost, abundant, biodegradable, and highly stable adsorbents [13]. Cellulose is an abundant natural polymer and is commonly found in wood, seeds, algae, and agro-industrial waste. The Moringa tree (*Moringa oleifera* Lam), a member of the Moringaceae family, can grow around the tropics. It is native to sub-Himalayan areas of northwestern India. It can be easily cultivated and adapts to semiarid climates, as it is a polyvalent tropical tree. In Michoacan, Mexico, the generation of residual biomass product from its plantation along the Pacific coast has been reported, with an average of 300 to 500 kg per hectare. This waste from leaves, stems, and branches concentrates wasted cellulose in large amounts [14,15]. Among the various functional polymers exist cellulose nanofibers (NFCs). Such fibers are large flexible fiber structures consisting of alternating crystalline and amorphous domains in a net-like structure. NFCs can be extracted from a cellulosic material, moderately degraded by chemical methods, thermal processes, and mechanical processes. Additionally, NFCs have been obtained from combined pulping Kraft process, acid hydrolysis, and ultrasonic methods [16,17].

The adsorption of metals by this type of material can be attributed to their structural compounds with various functional groups, such as carboxyl, carbonyl, sulfide, and hydroxyl. Many of these hydroxyl groups allow chemical modification and improve adsorption performance [18]. Cellulose tends to form an aggregate structure due to the hydrogen bonds being present, limiting adsorption; hence, modification of the cellulose structure and surface can help to avoid adsorption restraints. One of these modifications involves impregnation with metallic nanoparticles. Such a change can enhance adsorption properties in the biopolymer [19]. It has been reported that many metal oxide nanoparticles and other inorganic nanoparticles (i.e., zeolite nanoparticles) effectively and quickly remove metal contaminants in wastewater treatment processes [11,20].

The appearance of iron nanoparticles in remediation is attributed to their low toxicity and redox capacity when reacting with water. They have a large surface areas and high reactivity [21]. The use of iron nanoparticles has been reported in different carbon-based materials, such as starch and biopolymers, as well as in mineral adsorbents, such as clays. These materials act as supports for obtaining nanocomposites [22–26]. Moreover, functionalization with organic solvents helps to mitigate nanoparticles' agglomeration on the composite and improves dispersion. Different modifiers are used to abate nanoparticles' mobility in water, such as carboxymethyl cellulose or cellulose, since they are negatively charged molecules. These nanoparticles (NPs) are generally considered to be the most mobile in aqueous solutions due to electrostatic repulsion [27].

Several processes have been utilized to prepare nanoadsorbents. These are often considered as time-consuming processes, have high reagent requirements, and release toxic substances into the environment [28]. Otherwise, nanoparticles synthesized by plant products or extracts are more stable. These green syntheses are more manageable than conventional techniques. Such ecological approaches are cost-effective, simple, and sustainable and do not involve any toxic agents [29]. Different green synthesis routes use agro-industrial wastes, biopolymers, solvent replacement, plants, microorganisms, etc. [30]. Nanoparticles can be incorporated into the biopolymer through different mechanisms, such as chemical coprecipitation, to obtain the final composite material. Still, the use of plant extracts (organic compounds) can influence the reduction process. They can also stabilize the nanoparticles, promoting bonding to the biopolymer [31].

Fruits, seeds, stem, and leaf extracts from different plants contain useful polyphenols for metal reduction. These substances have been researched as bioreducing agents to synthesize nanoparticles, such as *Vitex negundo* L., *E. condylocarpa*, and *Amaranthus dubius* [32–35]; including *Rumex acetosa* [36], *Eucalyptus globulus* [37], *Mukia maderaspatana* [38], *Camellia sinensis* [39], *Rosemarinus officinalis* [40], *Citrus maxima* [41], *Azadirachta Indica* [30,42], green tea [43], eucalyptus [44], and *Canna indica* [21]. Additionally, waste materials such as banana peel and citrus juice waste have also been used.

Green plant leaves have recently been studied for the eco-friendly synthesis of iron nanoparticles, using Fe(II) or Fe(III) chloride solutions as precursors [30]. This synthesis is possible because these plants contain bioactive components, mostly polyphenols, that act as reducing and capping agents. Moreover, several applications and syntheses of metal oxide nanoparticles, particularly for iron, have been reported [45–49]. Jitendra et al. [50] reported that *A. indica* leaf extract assisted in the green synthesis of highly crystalline α-Fe_2O_3 nanomaterials with well-defined unique morphologies. Similarly, the green-synthesized mesoporous α-Fe_2O_3 had a surface area four times larger than the commercial α-Fe_2O_3 nanoparticles [39]. Moringa leaf contains various photochemical type-like flavonoids, such as polyphenols, rutin, kaempferol, chlorogenic acid, quercetin-malonyl-glucoside, glucosinolate, and isothiocyanates, with high antioxidant capacities. These are an alternative reducing agent for synthesizing iron oxide NPs [51,52].

Therefore, the present study aims to evaluate the iron nanoparticles and cellulose nanofibers (FeNPs/NFCs) performance for the removal of Cd(II) and Pb(II) from aqueous solutions and to examine the structure of the composite obtained from the cellulose nanofiber's (from branch wood residues) contact with iron nanoparticles (from green synthesis with $FeCl_3$ and leaf tea extract). Furthermore, the influence of contact time, temperature, and pH on adsorption experiments was determined, as were the adsorption mechanisms and thermodynamic, kinetic, and isothermal parameters of the studied systems.

2. Materials and Methods

2.1. Preparation of FeNP/NFC Composite

Large amounts of wood residues obtained from the pruning of the Moringa tree were collected from an orchard located in the municipality of Nueva Italia in the State of Michoacán, Mexico. These wood residues were used for cellulose extraction by Kraft pulping, followed by acid hydrolysis.

The cellulose nanofibrils (NFCs) were obtained using a high-intensity ultrasonication technique combined with cryo-crushing with liquid nitrogen. Wood chips from *Moringa oleifera* Lam. were cooked by Kraft pulping in a Kamir digester (METROTEC, model LB-16) with a capacity of 15 L and a speed of 5.16 r.p.m. The Kraft Pulping process was carried out with the following operating parameters: the temperature ranged from 160 to 170 °C with a boiling time of 20–30 min, a white liquor with sulfidity levels between 20 and 27% was used, using 200 g of wood chips (dry basis).

Chemical post-treatment to wood fibers by acid hydrolysis was performed with an H_2SO_4 solution 40% (*v/v*) at 80 °C for 2 h. The separation of fibers was carried out using a high-intensity ultrasonication technique combined with cryo-crushing with liquid nitrogen.

The mechanical cryo-crushing with ice crystal formation slashed the vegetal fiber wall and released wall fragments. The ultrasonic treatment was carried out for 40 min at 60 kHz, and then the material was dried in an oven. Mechanical fibrillation was performed using liquid nitrogen and applying high shear forces.

The synthesis of the composite material (FeNP/NFC) was carried out by putting in contact 4 g of cellulose (Kraft pulp) and 40 mL of leaf extract. Fresh *Moringa oleifera* Lam. leaves were collected and carefully washed with deionized water, and they were dried at room temperature with constant ventilation. Then, 20 g of dried leaves sample were mixed with 150 mL distilled water at 60 °C for 45 min. The supernatant was filtered with a Whatman filter paper to produce the leaf extract, and was stored at 4 °C in the refrigerator. A 0.5 M solution of $FeCl_3.6H_2O$ was subsequently adjusted at pH 8, using 0.1 N HCl and 0.1 N NaOH solutions. The leaf extract (pH 5.6) was added dropwise to the $FeCl_3$ solution with continuous stirring at 60 °C for 180 min. The modified material FeNP/NFC was filtered and washed several times with distilled water to eliminate any excess of reactive components from the material; the modified material was allowed to dry and it was stored in a desiccator.

2.2. Characterization of FeNP/NFC Composite

Different methods were used to perform the characterization of Kraft pulp and composite material in order to determine their morphologies, semiquantitative elemental properties, and surface properties. Scanning Electron Microscopy (SEM) images were obtained using a JEOL JSM IT300LV microscope (Tokyo, Japan).

Fourier Transform Infrared Spectroscopy (FTIR) was used to examine the changes in the functional groups induced by the adsorbent synthesis and the adsorption process. The samples were analyzed in a Bruker® Tensor 27 FTIR spectrophotometer (Bruker Optics Inc., Billerica, MA, USA).

The zeta potential (ZP) was used to measure the electrical potential on the adsorbent's surface. From the values of the zeta potential at different values 3 to 10 pH, the surface acidity or basicity and the isoelectric point were determined [16]. The FeNP/NFC material's zeta potential was measured with a Nano Brook 90 Plus Zeta instrument.

X-ray Diffraction (XRD) measurements were conducted to determine the presence of the cellulose crystalline phase in the samples, using a Rigaku Ultima IV (Rikagu, Tokio, Japan). The diffracted intensity of the Cu-Kα (λ = 1.54 Å) was measured in a 2θ range. Data analysis to identify crystalline and amorphous phases was carried out using Match V. 1.10[a] 2003–2010 Software (Crystal Impact, Bonn, Germany).

The FeNP/NFC composite oxides were analyzed on an energy dispersive X-Ray fluorescence spectrometer model Bruker S2PUMA with an Ag tube. Samples were analyzed to define the form of oxides.

2.3. Adsorption Experiments

2.3.1. Kinetics

Batch-type experiments with FeNP/NC were performed to determine Cd and Pb removal. Samples with 10 mL aliquots of a 2 mg/L metal solution were put in contact with 0.05 g of composite material in plastic flasks. The pHs of the initial solution for Pb and Cd were 2 and 3, respectively. The solutions' pHs were adjusted to and maintained at 5 (by adding 0.01 M HCl or 0.05 M NaOH to the solutions) due to the cationic chemical species (II) present in the solution. The flasks were shaken, separately, at 100 rpm and 25 °C. The solutions' concentrations were 2 mg/L for both $Pb(NO_3)_2$ and $Cd(NO_3)_2{\cdot}4H_2O$. The contact times ranged from 5 to 150 min to acquire the equilibrium time. After the contact time was achieved, the supernatants were separated by filtration, and the residual solution was analyzed for each metal by Flame Atomic Absorption Spectrometry (FAAS) (model Perkin Elmer® AANALYST 200, Waltham, MA, USA). The solutions were refrigerated at 4 °C and stored in amber bottles (plastic and glass) to avoid precipitation and oxidation during analysis. The experiments were performed in triplicate to determine reproducibility.

The Cd and Pb adsorption concentrations at equilibrium time during adsorption were calculated by:

$$q_t = \frac{(C_o - C_t)V}{m} \quad (1)$$

where q_t is the amount of ion adsorbed, at a time (t), per weight of adsorbent (mg/g); C_o is the initial concentration of heavy metal (mg/L); C_t is the concentration of heavy metal at that equilibrium time (mg/L); V is the volume of solution (L), and m is the mass of the adsorbent (g).

A batch removal system requires information about the optimum conditions that can only be acquired from kinetic models. Moreover, adsorption kinetics studies and their adjustment to empirical models allow the evaluation of removal mechanisms and are fundamental for selecting optimal design parameters for future effluent treatments. The data obtained from the kinetics tests were fitted to the Elovich, Lagergren (pseudo-first-order), and pseudo-second-order kinetic models by nonlinear regression analysis using Statistica 7.0 software. Such kinetic models were used in this research due to their wide use and acceptance in heavy metals removal studies.

The general expression of the pseudo-first-order rate, also known as the Lagergren model, is represented by the following equation [53].

$$q_t = q_e\left(1 - e^{-K_l t}\right) \quad (2)$$

where K_L is the Lagergren rate constant (1/min), q_t is the amount of ions adsorbed, at a time (t), per weight of adsorbent (mg/g), and q_e is the amount of ions adsorbed at the equilibrium (mg/g).

The pseudo-second-order model is based on the assumption that the rate-limiting step may be chemisorption [54]. Alternatively, the pseudo-second-order model is expressed in its linear form as follows:

$$q_t = \frac{K_2 q_e^2 t}{1 + 2K_2 q_e t} \quad (3)$$

where K_2 is the pseudo-second-order rate constant for adsorption (g/mg min), q_t is the amount of ions adsorbed, at a time (t), per weight of adsorbent (mg/g), and q_e is the amount of ions adsorbed at the equilibrium (mg/g).

The Elovich equation is represented by the following [55], commonly used in the kinetics of the chemisorption of gases on solids:

$$q_t = \frac{1}{b}\ln(1 + abt) \quad (4)$$

where q_t is the amount of ion adsorbed, at a time (t), per weight of adsorbent (mg/g), q_e is the concentration of solute removed at the equilibrium per weight of adsorbent (mg/g), K_L is the pseudo-first-order kinetic constant (1/min), K_2 is the pseudo-second-order rate constant of sorption (g/mg.min), and a and b are the Elovich constants related to the initial adsorption rate (mg/g min) and desorption rate (g/mg), respectively.

2.3.2. Isotherms

Adsorption isotherms were performed with Cd and Pb aqueous solutions at different concentrations to determine the systems' equilibrium parameters. Plastic vials were used to put 0.05 g of FeNP/NC in contact with 10 mL of Pb and Cd solutions, separately, at different concentrations, ranging from 5 to 500 mg/L. Then, the vials were placed in a thermostat-adjusted water bath agitator. They were shaken at 100 rpm at different temperatures (25, 30, and 40 °C). All experiments were performed in triplicate. According to the chemical equilibrium diagram for cation ions in an aqueous solution, the pH values were selected. Cd ions predominate at pH values between 2 and 8 and Pb ions with pH values between 3 and 5.5. The pH 5 value was then set and adjusted with 0.01 M HCl and 0.05 M NaOH solutions, as required, before the adsorption experiments.

The experimental data from sorption isotherms of Pb and Cd were fitted to the following isotherm models by nonlinear regression analysis. The equation that expresses the Freundlich model is:

$$Q_e = K_f C_e^{\frac{1}{n}} \quad (5)$$

where Q_e is the adsorption capacity of Pb(II) and Cd(II) of the adsorbents (mg/g), C_e is the equilibrium concentration of the metal ion in solution (mg/L), K_f is the equilibrium constant indicative of adsorption capacity, and n is the adsorption equilibrium constant whose reciprocal is indicative of adsorption intensity. The Freundlich model assumes that the adsorption process happened on heterogeneous surfaces [56].

Langmuir model could be represented by Equation (6) [57]:

$$Q_e = \frac{Q_0 K_L C_e}{1 + K_L C_e} \quad (6)$$

where Q_0 represents the maximum monolayer adsorption capacity of Pb and Cd, and K_L is the Langmuir constant (L/g). The Langmuir model is established based on forming a complete monolayer on the surface (mg/g).

Langmuir–Freundlich model is represented by Equation (7) [58]:

$$Q_e = \frac{K_{LF} C_e^{\frac{1}{n}}}{1 + a_{LF} C_e^{\frac{1}{n}}} \quad (7)$$

where K_{LF} and a_{LF} are empirical constants.

2.4. Thermodynamic Studies

The thermodynamic results were calculated from isotherm data of Pb and Cd at 25, 30, and 40 °C. The thermodynamic parameters were estimated to analyze the influence of temperature on metal ion adsorption, such as Gibb's free energy change ΔG (kJ/mol), enthalpy change ΔH (kJ/mol), and entropy change ΔS (J/mol K) [4,59], using the following thermodynamic equations:

$$K_c = \frac{C_{ad}}{C_e} \quad (8)$$

$$C_e = C_i\,(1 - F_e) \quad (9)$$

$$C_{ad} = C_i\,F_e \quad (10)$$

$$K_c = \frac{F_e}{1 - F_e} \quad (11)$$

$$\Delta G^\circ = -RTlnK_c \quad (12)$$

$$\Delta H^\circ = R\left(\frac{T_1 T_2}{T_1 - T_2}\right)\ln\frac{K_{c1}}{K_{c2}} \quad (13)$$

$$\Delta S^\circ = \frac{\Delta H^\circ - \Delta G^\circ}{T} \quad (14)$$

where R = 8.314 J/mol K is the universal gas constant; K_c (mL/g) is the equilibrium constant; C_e is the concentration of the metal in the solution at equilibrium (mg/L); C_i is the initial concentration of the metal in the solution at equilibrium (mg/L); F_e is the fractional conversion of the sorption at equilibrium, and T is the thermodynamic temperature (K).

Van't Hoff's equation [59] allowed us to obtain the ΔH° and ΔS° values graphically:

$$lnK_C = \frac{-\Delta H^\circ}{R\ x\ T} + \frac{\Delta S^\circ}{R} \quad (15)$$

A graph of lnK_c on the abscissa axis and $1/T$ on the ordinate axis should be linear, and the intercept would be equivalent to $\Delta S^{\circ}/R$, while the slope would be numerically equal to $\Delta H^{\circ}/R$.

3. Results and Discussion

3.1. Characterization of FeNP/NFC Composite

As shown in Figure 1, the surface morphology is significantly different before and after NFC impregnation with iron nanoparticles. After the hydrolysis and cryo-crushing process, NFC exhibited a cavernous network structure that has a smooth surface. Figure 1a,b, show the formation of several clefts or folds, which will help distribute the nanoparticles on the support material. The spaces between the microfibers collapse for wood and plant cellulose sources due to water molecules' outflow. When the microfibers dry, all the hydrogen bonds between the fibrils are displaced, forming weak links. It is essential to indicate the effect of pH on the material because hydrolysis was generated in an acidic medium. The concentration of hydronium ions incorporated into the material increased and, therefore, they are attributed to agglomeration behavior [60,61]. Cellulose nanofibers tend to aggregate due to hydrogen bonding between the OH and COOH- groups [62,63].

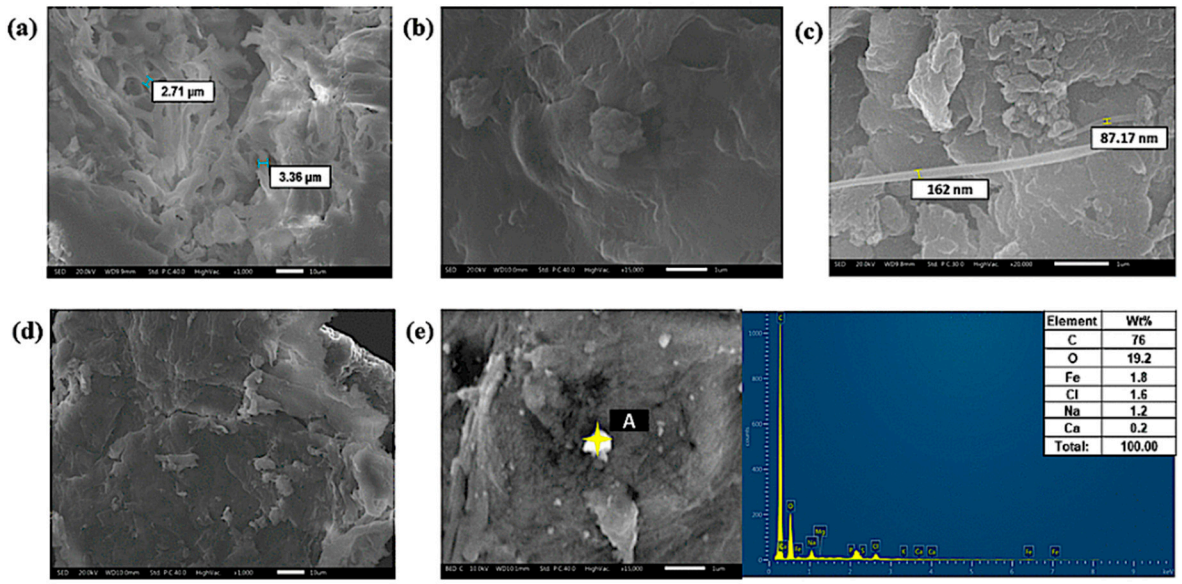

Figure 1. Scanning electron microscopy (SEM) micrographs of Cellulose nanofibers (NFCs): (**a**) X1000, (**b**) X15,000, (**c**) X20,000; iron nanoparticles and cellulose nanofibers (FeNPs/NFCs): (**d**) X1000, (**e**) X1500.

The cryo-crushing process formed ice crystals that helped to slash vegetal fiber and expose more surfaces, which allowed access to chemical activation of various functional groups. Because of nanofibers' exposure (Figure 1c), it can be established that the mechanical cryo-crushing and ultrasonic treatment were suitable for defibrillation of Moringa's Kraft pulp. The average diameter of nanofibers reported in other studies ranged from 50 to 100 nm, depending on the cellulose source [63–66]. In this case, the nanofibers' diameters ranged from 80 to 160 nm, as shown in Figure 1c, indicating nanofibers' presence. These nanofibers are not clearly seen in Figure 1a,b due to the micrographs' magnification. However, a nonhomogeneous accumulation of fibers can be observed in these micrographs (Figure 1a,b), which can also be denominated as microfibrillated cellulose (depending on the size and production process), consisting of cellulose nanofibers and nanofiber bundles [67,68].

Moreover, an increase in cellulose crystallinity has also been reported in NFC production from various sources [63,67]. In this case, such an increase was observed after the Moringa's NFC synthesis process, compared to the Kraft pulp cellulose crystallinity, due to the breaking down of the hierarchical structure of the cellulose into individualized

nanofibers of high crystallinity, with a reduction in amorphous parts [67]. The crystallinity of the Moringa's NFC will be discussed further below. Furthermore, FTIR analyses of several NFC samples from different sources proved that chemical treatment also led to partial removal of hemicelluloses and lignin from the fibers' structures. Still, the molecular structure of cellulose remained unchanged after chemical and mechanical treatments [64,67]. This behavior was also observed in the NFC from Moringa and will also be discussed further. Based on the above, the presence of cellulose nanofibrils in the Moringa composite can be confirmed.

In Figure 1d,e, micrographs of FeNP/NFC are observed. The surface showed a distribution of small particles which are related to NPs. Results for punctual Energy Dispersive X-Ray Spectroscopy (EDS) analysis (point A in Figure 1e) indicate high concentrations of carbon (C), oxygen (O), iron (Fe), chlorine (Cl), sodium (Na), and calcium (Ca), Figure 1e. Chlorine comes from the reactive solution used in FeNP/NCF preparation. The results indicate a certain percentage of Fe adhered to the surface, which is related to the synthesis of NPs. The alkaline pH system adjusted in the synthesis of nanoparticles helps incorporate hydroxyl groups (–OH) and NPs to the matrix. Hemicelluloses that still partially persist in the structure can inhibit nanofibrils' coalescence during the synthesis of iron nanoparticles. The formation of several slits is observed, which helped distribute the nanoparticles on the support material and capture these ions [61].

The elemental mapping was performed to the FeNP/NFC samples after the adsorption process. In Figure 2a,b, the main elements present on the materials' surfaces are carbon and oxygen in a higher proportion in weight, and low concentrations of dispersed forms of Cd and Pb. The sulfate (S), Ca, and Fe compounds contribute to Cd aggregates' adsorption on the surface of the material observed at various sites. Sodium comes from cooking liquors of the Kraft pulping process: NaOH, NaS, and Na_2CO_3. Calcium and potassium are the main elements present in the wood. The sample's composition with adhered particles of Cd is shown in Figure 3b at 5000×, where the spot analysis indicates solid Cd particles. The results demonstrate the presence of Cd at around 11% (*w*/*w*), forming various phases on the material. The sample analysis shows a decrease in Fe (with values <0.15%) compared to the samples before Cd adsorption, indicating a possible ion-exchange sorption mechanism. The spot analysis of the sample that adsorbed Pb (Figure 3a) reached a concentration near 1.05% (*w*/*w*). The carboxylic acids, phenols, and alcohols on the surface of the adsorbent were protonated, and the surface was negatively charged, allowing adsorption.

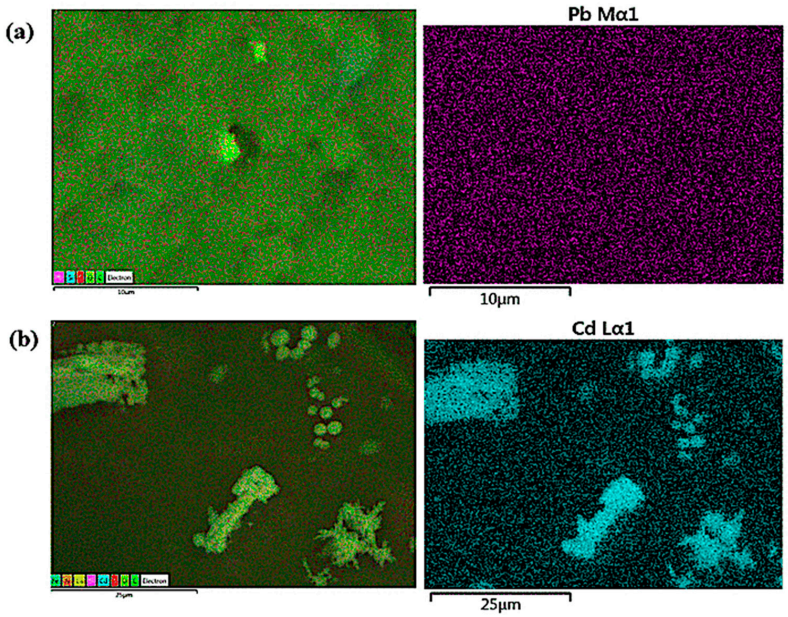

Figure 2. Elemental mapping of FeNP/NFC samples after adsorption of (**a**) lead (Pb) and (**b**) cadmium (Cd).

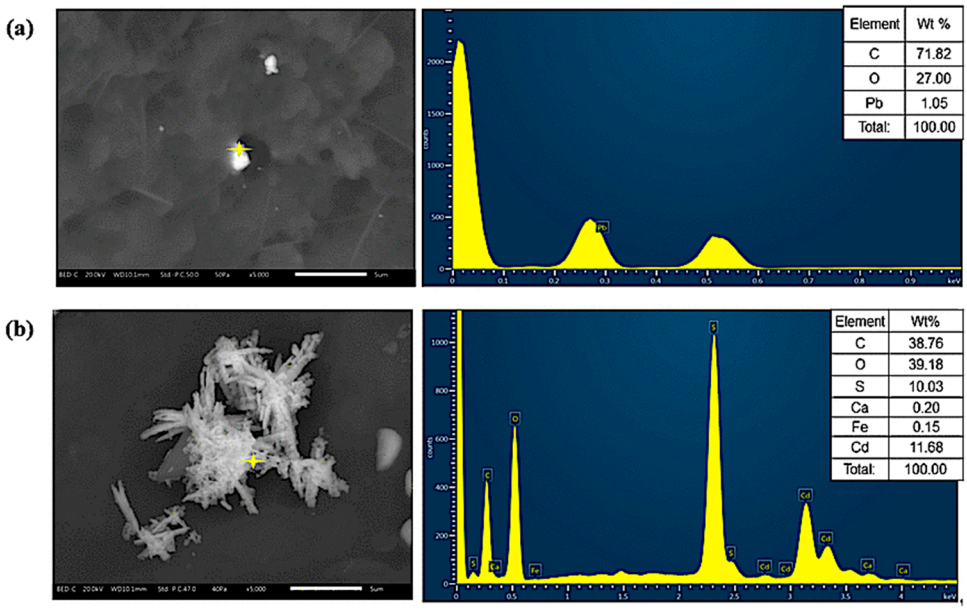

Figure 3. Spot analysis of composite samples after adsorption of (**a**) Pb and (**b**) Cd.

Figure 4 shows the FTIR spectra of NFC and FeNP/NFC. For both spectra, the broad peaks at 3406 and 3374 cm^{-1} are associated with -OH stretching vibration. The bands at 1636 and 1611 cm^{-1} are attributed to the water bending vibration. Displacement of these peaks is observed due to their intervention during the synthesis of the new material. In the case of the FeNP/NFC sample, the smaller peak at 2909 cm^{-1} corresponds to the -CH stretching of the aromatic rings and methylene ($-CH_2$), which are associated with functional groups involved in the green synthesis of nanoparticles. The appearance of a band at 1456 cm^{-1} can be assigned to a $-CH_2$ bending vibration and -OH deformation vibration, for the phenolic or alcoholic group.

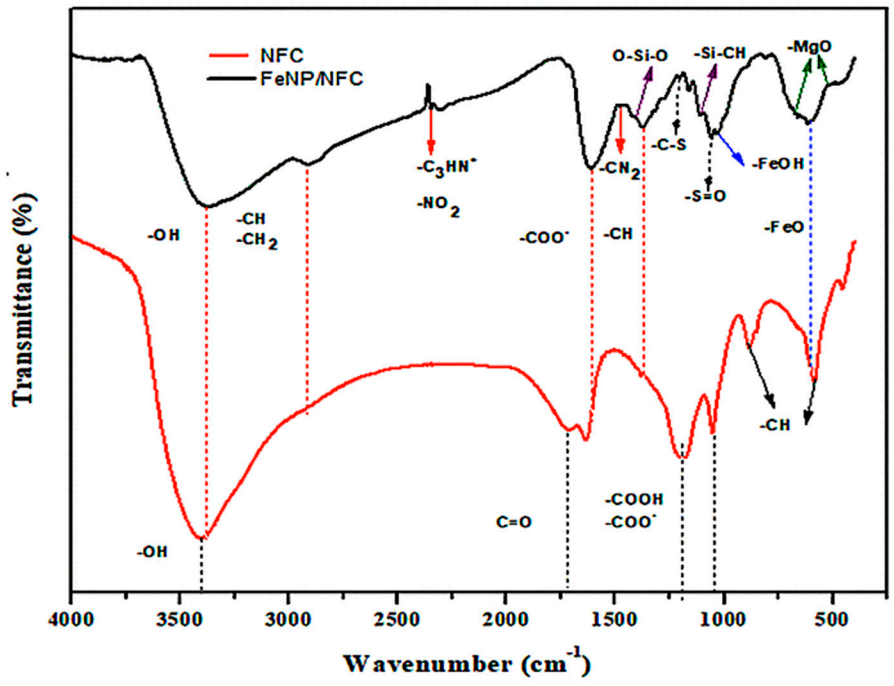

Figure 4. Fourier Transform Infrared Spectroscopy (FTIR) spectra of NFC and FeNP/NFC samples.

Significant changes were observed in the bands from 1500 to 1000 cm^{-1}. The bands from 1502 to 1418 cm^{-1} correspond to the aromatic elongation of C=C bonds and aromatic deformation vibration of C-C bonds. The stretching of carboxylic acids and esters peak is present at 1271 cm^{-1}. Ether and free alcohol C-O stretching can also be observed at the bands from 1000 to 1280 cm^{-1}. The adsorption peaks at 1161 and 661 cm^{-1} are attributed to asymmetric C-O-C and deformation of out-of-plane hydrogen of the C-H bond in the aromatic ring [69].

After the Fe nanoparticles' impregnation on NFC, some peaks' intensities increased in the spectrum of the FeNP/NFC composite (Figure 4)—mainly the bands that appeared in the region between 600 and 400 cm^{-1}, which correspond to Fe oxides. The FTIR spectrum of FeNP/NFC exhibited peaks at 1611, 1551, 1463, 1376, 1031, and 600 cm^{-1}. The broad peak at 601 cm^{-1} was attributed to stretching vibrations of Fe-O.

On the other hand, the O-Si-O and Si-CH functional groups were observed in the cellulosic material; thus, main peaks with stretching and bending vibrations from 1430 to 1100 cm^{-1} were noticed. The Si can also react with the noncellulosic components, where it can contribute to the Fe-O bond from 580 to 603 cm^{-1} due to the formation of the Fe-O-Si bond [70]. Furthermore, the peaks with lower intensities, at 511 and 675 cm^{-1}, such as -MgO, are related to other oxides present in the material. These sites intervened in the adsorption and were largely attributed to the wood's inorganic portion, and a smaller portion to the final material [71]

The peaks around 1376 and 1463 cm^{-1} increased their intensity; these are attributed to the -CH symmetric vibration of the polymeric matrix of NFC, mainly due to a strong hydrogen bond between the NFC groups and iron nanoparticles. The broad peak at 1031 cm^{-1} was associated with Fe-OH vibration; it indicates the incorporation of iron onto the surface [69]. The stretching vibration of O=S=O was observed at 1384 cm^{-1}; the C-S group was found at 1200 cm^{-1} and the S=O group was identified at 1053 cm^{-1}. These bands confirmed the presence of the sulfonic group. The effect of alkaline and acid treatments on cellulosic materials leads to surface activation with various functional groups such as -SH, $-SOH_2$, -SO, $-(CH_3O)_2SO_2$, and C-S, which can help in the adsorption process [4,56]. Bands at 2340, 2346, and 1478 cm^{-1} are typical of N vibrations, such as $-NO_2$, C_3HN^+, and CN_2; these groups were formed by the cellulose synthesis and extraction [72].

The Fourier Transform Infrared Spectroscopy (FTIR) analysis reveals (Figure 4) that the FeNP/NFC was esterified during the synthesis process at 1721 cm^{-1}; this band is usually attributed to C=O stretching vibration, and a decrease in this band was observed for the FeNP/NFC sample. A new weak absorption peak appeared at 1427 cm^{-1}, which could be attributed to the bending vibration of OH in carboxyl groups. On the other hand, a large amount of -COOH groups had been introduced to cellulose after the modification; these groups possess strong adsorption properties for heavy metal ions [73].

Figure 5 shows the FTIR spectra of FeNP/NFC adsorbent after Pb adsorption (PbRM) and after Cd adsorption (CdRM). It was observed that metal adsorption generated slight displacements in some bands and significant changes in the band frequencies of groups such as -OH, -COO-, C=O, C-O, and C-O-C; this suggests that such ionizable functional groups on the adsorbent surface can bond with the metal ion. For CdRM and PbRM, the stretching vibration peak of C-H observed at bands from 2800 to 3000 cm^{-1} disappeared, indicating that C-H may participate in the cross-linking reaction. Moreover, at the 1630 cm^{-1} wavenumber, band intensity changes can be attributed to the $Pb(NO_2)$ stretching vibration. Therefore, it can be established that amine groups in FeNP/NFC play an essential role in lead adsorption on this material by sharing one electron pair of the nitrogen atom with the Pb ions. The decrease in free carboxylic acid, iron oxide, iron hydroxides, amide, nitrogen dioxide, magnesium oxide, sulfur groups, and other possible sites indicates the same type changes upon sorption of Pb and Cd ions.

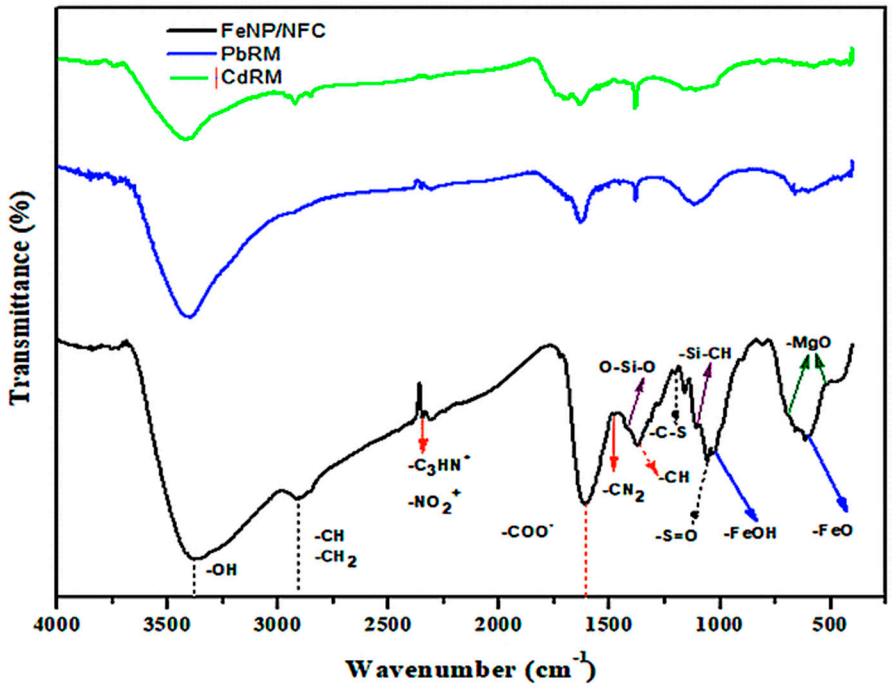

Figure 5. FTIR spectra of FeNP/NFC, adsorbent after Pb adsorption (PbRM) and after Cd adsorption (CdRM).

The zeta potential (ZP) value of FeNP/NFC increased from −11 to −23 mV; this lower negative value is due both to the polyphenolic components present in the extract during the synthesis of the material and also to the cellulose structure of the support material for the Fe nanoparticles (Figure 6) [34]. Different modification strategies create ionic groups on the surfaces of NFCs. Carboxymethylation, oxidation, and sulfonation are three routes that can add ionic groups on the surface of the cellulose. Carboxymethylation causes surfaces to be negatively charged, promoting stable suspension from carboxymethylated fibers. The oxidation process includes hydroxyl groups, which oxidize to aldehyde groups, followed by carboxyl groups. Sulfonation is considered as a way to induce an anionic charge on the surface with different functional groups such as -SO, -SH, and $-HSO_3^-$ [74,75].

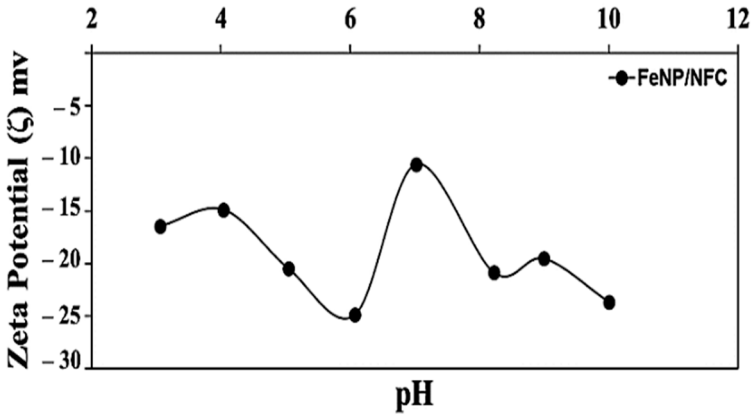

Figure 6. Zeta potential (ZP) of FeNP/NFC composite.

There is no evidence of an isoelectric point in the sample, which confirms that charge dissociation is virtually independent of pH. Under acidic conditions, as the pH decreases, the -COO- groups are converted to -COOH resulting in a lower density of surface charge, and therefore a reduction in mobility. Additionally, an increase in pH did not change the particle mobility significantly. In all of the pH ranges, the Zeta potential values were

negative; therefore, it can be considered that the pH does not affect the surface loading properties of the material. Particles with low zeta potential have tended to agglomerate, while particles with high zeta potentials have been electrically stable.

On the other hand, the crystalline structure of cellulose is one of the most studied structural problems in polymer science, and its accurate description of the crystal structure remains a topic of discussion [76,77]. Therefore, an analysis of the crystal structure by XRD was carried out to determine the composite material's crystalline state.

As shown in XRD patterns (Figure 7), there is strong diffraction at 14.63°, 16.7°, and 22.42° of FeNP/NFC, corresponding to the (101), (10 ī), and (002) crystalline planes for cellulose II, into the sample. The acid hydrolysis and cryo-crushing methods destroy the stable hydrogen bonds, generate free hydroxyl groups, and increase cellulose reactivity [73]. They were indexed in the structure of cellulose (JCPDS No. 50-2241). The diffraction intensity was weak for the (101) and (10 ī) crystal planes. These two peaks overlap with each other because they have a lower amount of lignin and hemicellulose, resulting from the adsorbent's synthesis process.

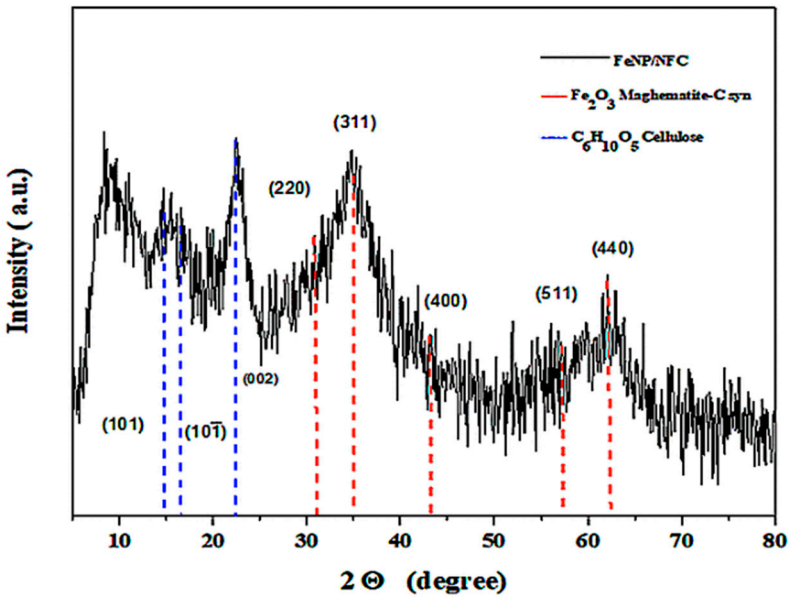

Figure 7. X-ray Diffraction (XRD) patterns of the FeNP/NFC, prepared with Moringa leaf extract.

It is difficult for chemical reactions to take place in the crystalline region because of its stable structure. Hence, it becomes an easily accessible and penetrable amorphous structure, increasing iron nanoparticles' introduction [4,73]. XRD patterns show peaks related to amorphous and crystalline compounds (Figure 7). The nanoparticles in the material presented peaks at around 30° to 62°, which could be due to crystalline materials on organic matter.

The iron oxide phase in FeNP/NFC shows some intense XRD peaks—identified as maghematite (Fe_2O_3). These peaks and indices were 30.79° (220), 35.63° (311), 43.51° (400), 57.22° (511), and 62.79° (440), as can be observed in Figure 7. The diffraction peaks belong to iron oxide maghematite-C syn (No. 00-024-0081) with a rhombohedral structure. Different amorphous materials impregnated with nanoparticles have been reported, finding that the iron nanoparticles prepared with green tea extract were efficient in different aspects [34]. The polyphenolic compounds from tea do not possess a reduction potential negative enough to reduce from Fe^{3+} to Fe^0 but can reduce Fe^{3+} to Fe^{2+}, forming oxide/hydroxide nanoparticles.

The Energy Dispersive X-ray Fluorescence (EDXRF) analysis is shown in the spectrum of Figure 8. The peaks around 0.8, 6.4, and 7.05 keV are related to the Fe binding energies. Therefore, the EDXRF spectrum for Fe_2O_3 from the FeNP/NFC material, synthesized with

aqueous extract of Moringa leaves, confirmed nanoparticles' presence. The number of radicals present in the hybrid sample revealed the photocatalytic activity of the nanoparticles. The other intense peaks shown in the EDXRF spectrum are marked as salts' structures derived from the extraction of the cellulose and its initial composition from the raw material derived from Moringa wood (Figure 8). The signal peak at 2.98 keV is assigned to silver (Ag), derived from its presence on the sample holder and tube in the instrument employed for the analysis; hence, the peak of iron looks smaller than silver. Potassium is essential for the growth of the tree, which can be seen in the graph's 3.16 keV intensity. The EDXRF spectrum analysis indicates that the sample has a composition of approximately 32.81% Fe_2O_3 and is only one of the existing oxide groups in the material (Table 1). According to this result, the weight percent of metal oxides on cellulose increased, confirming that the iron nanoparticles were successfully incorporated. Other than iron, different compounds were identified, such as MgO, SiO_2, P_2O_5, SO_3, and Cl (Table 1). Inorganic material in wood is found as carbonates, oxalates, silicates, phosphates, and sulfates; or organized as carboxyl groups in the cellulosic materials [78].

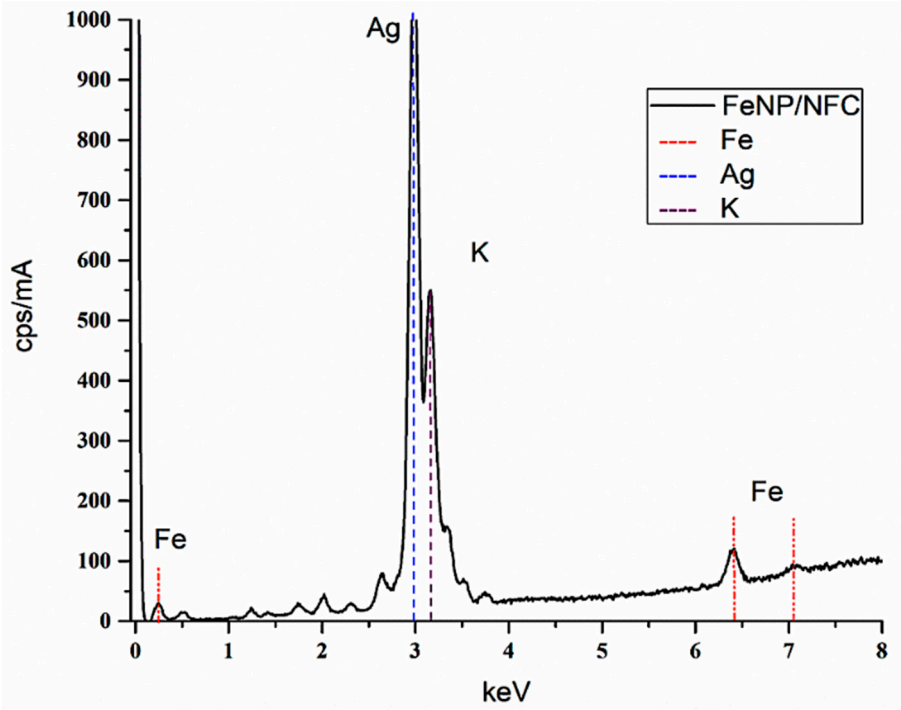

Figure 8. Energy Dispersive X-ray Fluorescence (EDXRF) spectrum of the FeNP/NFC composite.

Table 1. Composition of oxide groups in iron nanoparticles and cellulose nanofibers (FeNPs/NFCs).

Formula	
Concentration (%)	
Formula	**Concentration (%)**
MgO	13.55
SiO_2	20.65
P_2O_5	24.04
SO_3	3.68
Cl	5.26
Fe_2O_3	32.81

Generally, tropical woods contain inorganic salts of calcium, potassium, and magnesium [78,79]. Mineral transport into the plants can occur through natural routes from the soil, where minerals are in abundance. Silica, phosphorus, magnesium, and potassium

components of biomass contribute to the plant´s rigidness, growth, and posture [78,80,81]. Sulfur oxide is attributed to cooking Kraft pulp in the composition of the reagents in the white liquor. Chlorine can be attributed to the reagent used ($FeCl_3$) in the nanoparticle synthesis process [82–84]. The inorganic substances found contributed to the various chemical reaction processes that took place during the synthesis of the composite, such as carboxymethylation, oxidation, hydrolysis, and sulfonation.

3.2. Adsorption Experiments

3.2.1. Kinetics

The adsorption kinetics results are shown in Figure 9. The adsorption kinetics of Pb(II) and Cd(II) ions in FeNP/NFC were significantly different. Cd's adsorption in the initial stage was very fast in the first 5 min, where 22% of the total cadmium elimination was obtained. Still, it gradually slowed down and finally reached equilibrium with a maximum efficiency of 32%. In the case of Pb, the adsorption capacity was slow in the first 5 min, rapidly increased between 5 and 20 min, and then slowed down—being more constant up to 75 min (with adsorption of 40%). This adsorption system had an efficiency above 58%. The equilibrium time was selected after 150 min for both cations, and it was ensured that the adsorption equilibrium was reached in later experiments.

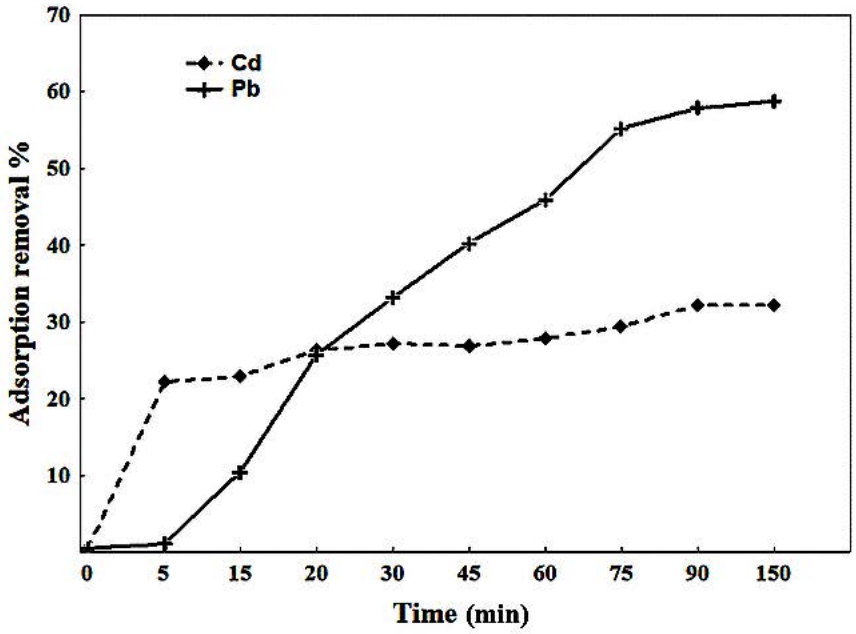

Figure 9. Cd and Pb adsorption onto FeNP/NFC composite as a function of time.

The adsorption phenomenon occurs at the surface, where the transport process and the diffusion of the adsorption are carried out between the film and the adsorbent. Moreover, the second phase is characterized by a slow adsorption rate due to the ions' slow diffusion and surface phenomena, which indicates the rate-limiting step and the type of adsorption governing the system. The effective adsorption area on the adsorbent's surface has many vacant bonding sites for the metal ions, and all resulted in easy adsorption. As adsorption proceeded, the concentration of metal ions and active sites decreased, resulting in a lower adsorption rate when the systems reached equilibrium.

The adsorption kinetic data were fitted to Pseudo-first-order, pseudo-second-order, and Elovich models. The correspondent parameters for each model are shown in Table 2. The high correlation coefficient values (R = 0.9858) obtained by the pseudo-first-order model for Pb adsorption indicates that sorption occurs exclusively at one site per ion and involves physisorption. This model suggests that the adsorption is superficial, and one solute molecule is adsorbed at one defined specific site. These sites were made up of the same

type of functional groups. For both adsorption kinetics, the calculated values (qe_{calc}) and experimental values ($q_{e\ exp}$) were similar. The theoretical or estimated values are considered the adsorption capacity calculated by kinetic modeling. Thus, $q_{e\ calc}$ from the pseudo-first-order model resulted in 0.1348 mg/g for Cd and 0.3401 mg/g for Pb. Adsorption capacity experimental values ($q_{e\ exp}$) were obtained from the experimental data graphs (Figure 9). Consequently, $q_{e\ exp}$ for Cd sorption was 0.1513 mg/g and 0.3109 mg/g for Pb.

Table 2. Parameters of kinetic models for cadmium (Cd) and lead (Pb) adsorption onto FeNP/NFC.

Model	Parameters	Metal Ions	
		Cd	Pb
	$q_{e\ exp.}$ [1] (mg/g)	0.1513	0.3109
Pseudo-first-order	K_L (1/min)	0.2445	0.0220
	$q_{e\ calc.}$ (mg/g)	0.1348	0.3401
	R	0.9197	0.9858
Pseudo-second-order	K_2 (1/min)	0.4486	0.0170
	$q_{e\ calc.}$ (mg/g)	0.2937	0.7781
	R	0.9611	0.9734
Elovich	a (1/min)	0.8112	0.00478
	b (mg/g)	59.077	2.4590
	R	0.9895	0.9204

[1] Obtained from experimental data.

The pseudo-first-order model can only be applied to describe the initial stage of adsorption. However, the pseudo-second-order model can predict the entire period of the adsorption behaviors. Therefore, the pseudo-second-order model can describe the adsorption behavior of the ions studied. In this model, the individual molecules join in two adsorption sites of the surface. They indicate that the sorption processes are entirely controlled by chemical processes and highlight their particularity in the electrical charge during equilibrium, such as the exchange of electrons or covalent forces.

According to the pseudo-second-order model constant (K_2), it can be observed that the adsorption rate is higher for Cd (K_2 = 0.4486 1/min) than for Pb (K_2 = 0.0170 1/min). This fact corroborates the differences found for both cations' adsorption kinetics, Cd, which implies a different equilibrium reaction for Cd compared to Pb. Cd's kinetic reaction rate indicates that it is only involved with the functional groups on the external surface. Pb's kinetics consist of multiple slow reactions between the outer surface and the material's internal pores. Additionally, the adsorption of Cd ions by the adsorbent was described with the Elovich equation (R = 0.9895). However, when the Elovich model fitted Pb data, low correlation coefficients were observed. This model indicates that the adsorbent's active sites are heterogeneous and exhibit different activation energies, based on a second-order reaction mechanism for a heterogeneous reaction process. Consequently, this model suggests that Cd removal occurs by a chemisorption process concerning the transfer or exchange of electrons, taking into account the metal's oxidation state and the possible formation of complexes involved in it [85].

3.2.2. Isotherms

Figure 10 shows the adsorption isotherms of Cd in FeNP/NFC at different temperatures. Considering the Langmuir, Freundlich, and Langmuir–Freundlich models presented, the three models had a good fit for the three different temperatures, with R values > 0.9700 (Table 3). However, in solid–liquid systems, many factors come into play, such as hydration forces, mass transfer, etc., which makes it more complicated to define equilibrium behavior in a sorption system, and obeying a single isotherm does not fully reflect the entire

adsorption process. Moreover, the isotherm's suitability may be affected by experimental conditions, mainly the solute's concentration range. Both Langmuir and Freundlich isotherms may adequately describe the same set of liquid–solid adsorption data at specific concentration ranges. The Langmuir–Freundlich isotherm model gives information about the adsorption on homogeneous and heterogeneous surfaces with the possibility of multilayer adsorption.

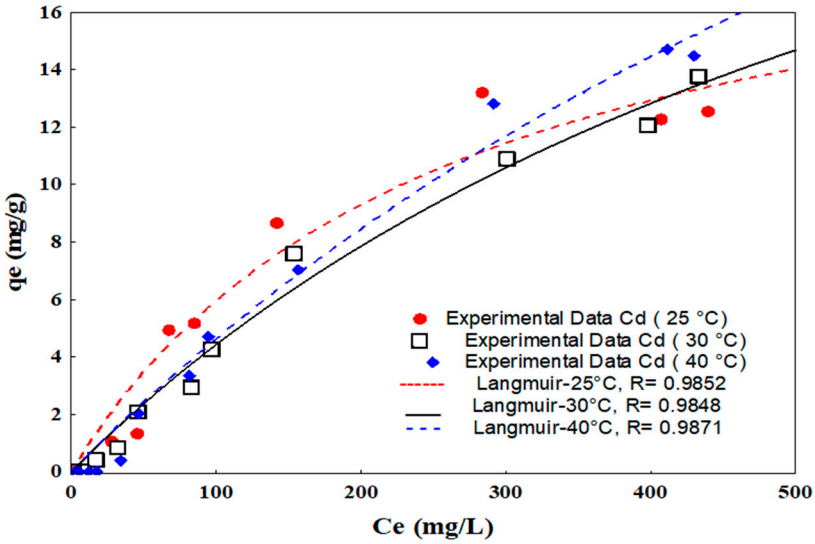

Figure 10. Cd adsorption isotherms onto FeNP/NFC composite at 25, 30, and 40 °C.

Table 3. Parameters of kinetic models for Cd and Pb adsorption onto FeNP/NFC.

Model	Parameters	Metal Ions					
		Cd			Pb		
		25 °C	30 °C	40 °C	25 °C	30 °C	40 °C
	$q_{e\ exp.}$ [1] (mg/g)	12.538	13.7377	14.4896	81.4064	89.2212	89.0882
Langmuir	$Q_{0\ calc.}$ (mg/g)	21.233	34.999	49.697	467.307	956.02	357.549
	b	0.0040	0.0014	0.0010	0.0131	0.0084	0.0263
	R	0.9789	0.9929	0.9924	0.9149	0.7274	0.7294
Freundlich	K_F (mg/g) $(L/mg)^{1/n}$	0.2601	0.0922	0.0775	4.1092	0.7209	1.4545
	n	1.5275	1.2117	1.1443	0.8916	0.4163	0.5055
	R	0.9617	0.9895	0.9891	0.9262	0.9180	0.8707
Langmuir–Freundlich	K_{LF} (mg/g)$(L/mg)^{1/nLF}$	0.8453	1.0635	0.2825	0.17961	0.3134	0.2995
	a_{LF} (mg/L)	1×10^{-4}	2×10^{-6}	3×10^{-6}	0.1394	0.1223	0.1511
	n_{LF}	0.4763	0.4052	0.6554	3.1486	3.0864	3.2310
	R	0.9234	0.8864	0.9731	0.9934	0.9390	0.9040

[1] Obtained from experimental data.

The Langmuir model was the one that best described all the isotherms of Cd at 25, 30, and 40 °C, with adsorption capacities of 21.233, 34.999, and 46.697 mg/g for each temperature, respectively. The Langmuir model was used to describe the monolayer adsorption at the adsorbent's surface, considering the similar types of vacancies and similar forces binding Cd molecules to the adsorbent's surface. The value of b in the Langmuir model suggests that the isotherm was favorable ($0 < b < 1$). In this context, the low b values reflect that adsorption is favorable: b > 1 is unfavorable, $b = 1$ is linear, $0 < b < 1$

is favorable or $b = 0$ is irreversible. In this case, the respective b values for each evaluated temperature indicate that the adsorption process was favorable [12,86]. The Langmuir equation is valid for monolayer sorption onto a completely homogeneous surface with a finite number of identical sites and little interaction between adsorbed molecules. This fact means that once a metal ion occupies a site, it cannot have another place for adsorption, so the adsorption behavior is gradually reflected in the different tested concentrations of Cd.

Lead (Pb) isotherm data were also fitted to the same models mentioned above. The results are shown in Figure 11. It was noticed that the Langmuir–Freundlich model best described such data at 25, 30, and 40 °C, according to their correlation coefficients (R), shown in Table 3. This model describes the equilibrium relationship between adsorbate binding and heterogeneous or homogeneous surfaces [72]. These surfaces have spaces with different forces, where the adsorbate molecules bind to the surface. The isotherm at high solute concentrations indicated a duality of both monolayer and multilayer adsorption [72]. This fact reinforces the idea that the governing mechanism is more complicated for Pb (II) than for the weak bond of Cd (II). As a result, a $Q_{0\ cal}$ value of 467.307 mg/g was obtained for the Pb system at 25 °C, and the $Q_{0\ cal}$ values at 30 and 40 °C were 956.02 and 357.549 mg/g, respectively, as shown in Table 3. Some discrepancies regarding Q_0 can be observed at 30 and 40 °C because of the relatively low R coefficients obtained in the Langmuir model's fittings in such cases. These results complement together with the Freundlich model, so the adsorption intensity (n) was always <1 for Pb adsorption cases (Table 3). These values ($0 < n < 1$) indicated favorable adsorption. These facts support that the lead adsorption was superficial and multilayered, considered as a heterogeneous adsorption type. Additionally, the adsorption mechanisms varied depending on the solution's concentrations. In this context, it is essential to emphasize that the FeNP/NFC composite can be considered highly efficient in removing Pb ions from aqueous solutions under these experimental conditions.

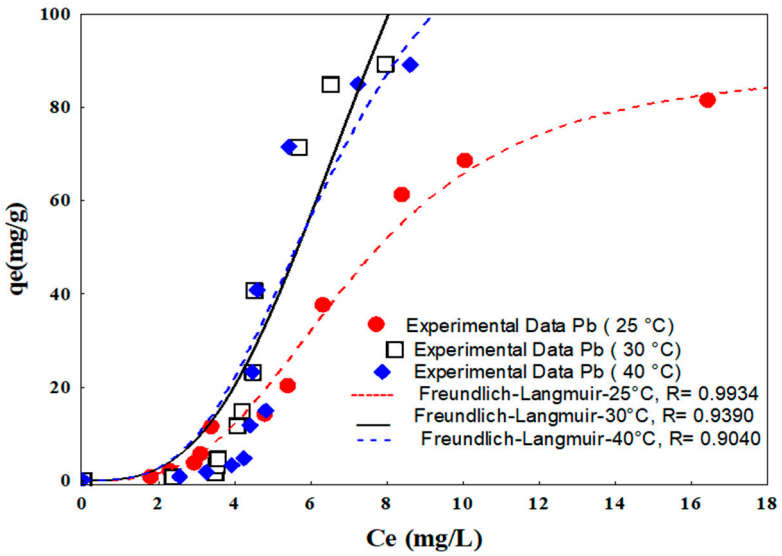

Figure 11. Pb adsorption isotherms onto FeNP/NFC composite at 25, 30, and 40 °C.

Polymers are heterogeneous materials containing sorption sites with various binding affinities and selectivities [45]. Hence, it can be suggested that the FeNP/NFC adsorbent has a heterogeneous surface, and Pb and Cd sorption onto this composite may present a multilayer behavior. The adsorption capacity of FeNP/NFC increased as the solute concentration rose until it reached the highest adsorption capacity. An increase in experimental adsorption capacity ($q_{e\ exp}$) was observed in high-temperature conditions (Table 3) for both ions.

Previous studies indicated three explanations in the absorption behavior of specific metallic ions towards the adsorbent: radio, electronegativity, and charge [87]. It can be inferred from the results that the order of heavy metal ion removal efficiency under the

experimental conditions was as follows: Pb(II) > Cd(II). The sizes of the ionic radius of the elements that are Pb (0.119 nm) > Cd (0.095 nm) should be taken into account. However, some studies conclude that the order of adsorption efficiency is due to the hydrated ionic radius of Pb (0.45 nm) < Cd (0.5 nm), highlighting a relatively smaller lead ion compared to cadmium. In aqueous solutions, ions form hydrate complexes with water, thus increasing the ionic size. Therefore, hydrated ions are transported to the surface of the material and diffuse into the pores [87–89].

The electronegativity is higher for lead ions (1.87–2.34) compared to cadmium (1.69). Phenomena, such as electrostatic interactions, covalent bonds, and ion exchange, could occur at the cellulose wall where cation bonding takes place. Adsorption or chelation involving hydroxyl functions, close to carboxylates or iron nanoparticles (-FeO, -FeOH), can increase the cation binding level [87].

The pH is an important parameter influencing the adsorption process at the water–sorbent interfaces. However, Pb and Cd's adsorption on this adsorbent is independent of the pH according to the zeta potential results of the material. As mentioned above, the solution's pH is reduced after the sorption process; this occurs because the deprotonation of the acidic functional groups of the adsorbent releases H_3O^+, allowing the metal cations to be adsorbed. The final pH value, obtained after the sorption experiments, was 3.6. Cd and Pb's removal by adsorption, reported in the literature, ranges from 3 to 8 for this type of sample [73,74]. Therefore, all further kinetic adsorption experiments were performed at a pH of 5.

Some polymers have shown that various surfaces are nonionogenic and acquire a negative charge in aqueous solutions. It has been shown that the electrokinetic charges of polymer surfaces become more negative as surface hydrophobicity increases. FeNP/NFC contains carboxyl (-COOH) and hydroxyl (-OH) functional groups as part of their polymer structures. Therefore, the negative electrokinetic charge acquired in the material can be explained by the dissociation of the mentioned functional groups [90]. The zeta potential was negative in all the pH values investigated; thus, this material can help remove Cd and Pb in some chemical species present in the solution. Both metals have the same charge (+2). It makes adsorption favorable in the system under study, though it depends on the chemical species present. Cadmium exists as a different form of Cd^{2+}, $Cd(OH)^+$, $Cd(OH)_2$, and $Cd(OH)_3^-$ at different pH values. At pH < 8.0, the predominant Cd species are Cd^{2+} [91]. Furthermore, Pb has a different form in aqueous solution at different pH values, such as Pb^{2+}, $Pb(OH)^+$, $Pb(OH)_2$, $Pb(OH)_3^-$, and $Pb(OH)_4^{2-}$. Pb^{2+} is the dominant species under acidic conditions because the Pb^{2+} and Cd^{2+} ions begin to hydrolyze and then form a minimal amount of other chemical species. Some of these species could be unfavorable for adsorption on negatively charged materials at pH < 3 in solution, so a value of 5 as the initial pH was selected for all adsorption experiments. The intense competition between hydronium ions and cations (Cd or Pb ions) decreases the metal ion interaction with the sorbent's binding sites by greater repulsive forces.

According to the Giles classification [92], sorption isotherms of Cd at 25, 30 and 40 °C can be included in S-type subgroup 2 (S-2). This fact indicates cooperative or complex adsorption with molecules that tend to be adsorbed in rows or groups. In celluloses, where free radical ions were involved in the adsorption, such as those present in this adsorbent, the solutes formed bonds with aromatic nuclei or their surroundings. Similarly, for the Pb isotherms at 25, 30, and 40 °C, the S-2 type can be described. The shapes of isotherms suggested one orientation of the adsorbed molecules stacked on the adsorbent's surface. The polymeric hydrocarbons in this material clearly cannot have simple surfaces because of their complex three-dimensional structures. Nevertheless, they produce S-curves. The cause is not, in this case, competition with water in the solvent, but it is possibly promoted by some form or interlocking of the adsorbed molecules [92,93]. Being classified in subgroup 2 indicates that monolayer capacity has reached its maximum. The plateau's height determines the surface cover for each solute molecule; additionally, electrostatic forces were involved in the adsorption. As seen in Figure 11, the length of

the plateau showed an exposed surface, which easily attracted Cd and Pb ions. In nearly all cases, the isotherms have the S-shape. The adsorption sites appear to be isolated and negatively charged atoms.

A comparison of the maximum experimental adsorption capacities with similar adsorbents are shown in Table 4 for Cd and Pb. Differences in experimental conditions have been considered when comparing with other adsorbents. The advantage of using FeNP/NFC as an adsorbent is significant, and it can be observed that, compared with the other materials, it is highly efficient for removing Cd and, especially, Pb ions.

The adsorption capacities of synthesized nanocomposites in this study can be compared to other available adsorbents. Prasher et al. [94] indicated that the Pb(II) adsorption capacity obtained for the red algae biosorbent was superior compared to Cd(II) under similar experimental conditions. In some studies, this sorption behavior was also explained by the concepts of ionizing radio, electronegativity, and ion charge.

Table 4. Cd and Pb adsorption capacities of different adsorbents.

Adsorbent	$q_{e\ exp.}$ (mg/g)		Temperature (°C)	pH	Adsorbent Mass (g)	Solution Volume (mL)	Reference
	Cd	Pb					
FeNP/NFC	12.538 13.737 14.489	81.406 89.221 89.088	25 30 40	5 5 5	0.05 0.05 0.05	10 10 10	This study
Magnetic Bauhinia purpurea (Kaniar) powders	0.83 0.86 2.20	14.14 1.02 1.35	25 30 40	5	2	50	[4]
Biochar (waste agro-industry) FeSO4·7H2O	38.3 to 75.3	179-311	25	5	0.04	20	[95]
Banana peels	5.71	2.18	25	3	1.5	50	[96]
Polymer-modified magnetic nanoparticles	29.6	3.103	25	1 to 8	0.05	50	[97]
Chitosan/iron oxide nanocomposite	4.106	3.795	25	3	0.05	20,000	[98]
Sugar beet pulp	0.98	1.00	25	5	0.4	20	[99]
Sawdust ($Fe3O_4$/SC)	63 22 25	– – –	27	6.5	0.4 1.2 2	50	[100]
Fe3O4 nanoparticles onto cellulose acetate nanofibers	–	44	27	6	0.1	50	[101]

Biochar from agro-industrial wastes (nut shield, wheat straw, grape stalk, grape husk, and plum stone) was evaluated by Trakal et al. [95]. The results indicated that this material was strengthened after Fe oxide impregnation, increasing Cd and Pb sorption capacities. Such higher capacities were attributed to the surface complexation of metals with carboxyl and hydroxyl functional groups. In this case, Pb's adsorption capacity was higher than that of Cd, with different experimental conditions.

3.3. Thermodynamic Parameters

The analysis of these parameters allows the estimation of the feasibility of the adsorption process and the effect of temperature. The results of ΔH and Δ*S* were obtained from the slope and intercept of the graph lnK_c versus $1/T$ (Figure 12), using isotherm data. Parameters ΔG°, ΔH°, and ΔS° for the metal ions adsorption with FeNP/NFC are listed in Table 5.

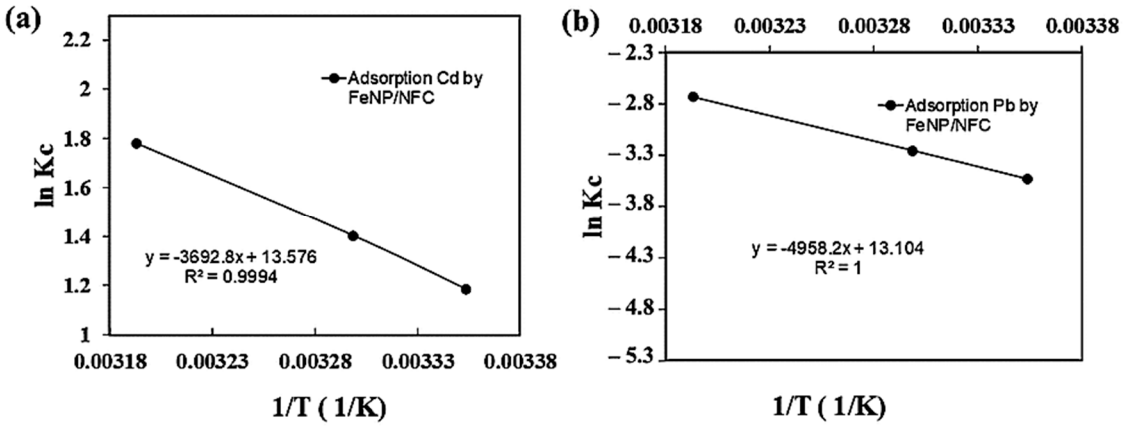

Figure 12. Van't Hoff's equation model for (**a**) Cd, and (**b**) Pb.

Table 5. Thermodynamic parameters for Pb and Cd adsorption on FeNP/NFC.

Metal Ions	ΔG° (kJ/mol)			ΔH° (kJ/mol)	ΔS° (KJ/mol K)
	25 °C	30 °C	40 °C		
Cd	−64.339	−64.904	−66.031	−30.701	0.1128
Pb	−73.704	−74.250	−75.339	−41.222	0.1089

The negative values of ΔG indicate a spontaneous reaction of the adsorption process for the FeNP/NFC. However, only a slight decrease in Pb and Cd maximum adsorption capacities was observed as temperature increased. Therefore, a large amount of heat was consumed for the Pb and Cd ions to transfer from water into the surface of FeNP/NFC [26]. The ΔH° results are negative for both cations, indicating that the adsorption process is exothermic; the values of $\Delta H^\circ < 0$ and $\Delta S > 0$ imply that it is spontaneous at all temperatures. The positive value of ΔS suggests an increased disorder in the system during the process of adsorption. A redistribution of energy between the heavy metals and FeNP/NFC occurred, which suggests increasing randomness with structural or solvation changes occurring at the solid/liquid interface [4]. Acidic functional groups in the adsorbent, such as carboxylic and carboxylate, decreased. The solvent–sorbent interactions were similar; therefore, the change in entropy decreased [59].

3.4. Adsorption Mechanism

A possible mechanism of nanoparticle formation is illustrated in Figure 13. Ferric chloride hexahydrate hydrolyzes to form the ferric hydroxide, releasing H^+. The leaves extract partially reduces the ferric hydroxide to form NPs. Small Fe_2O_3 crystals were formed and placed at the coordination sites in a monodisperse form on the carrier. Physical or thermodynamic principles can also contribute to nanocrystals' self-assembly [3]. They can provide heterogeneous coordination or nucleation sites needed to form complexes with the ion. The aldehyde groups of the extract oxidize the cellulose material's corresponding structures [102,103]. The predominant flavonoids and polyphenols identified in the Moringa leaf extracts include rutin, kaempferol or isorhamnetin, isothiocyanates, chlorogenic acid, and quercetin-malonyl-glucoside. All these processes contribute to metal ion reduction [39,52]. The free radical scavenging activity of *Moringa oleifera* Lam leaf has been reported to be higher than synthetic antioxidant counterparts such as butylated hydroxytoluene (BHT), rutin, and ascorbic acid [51].

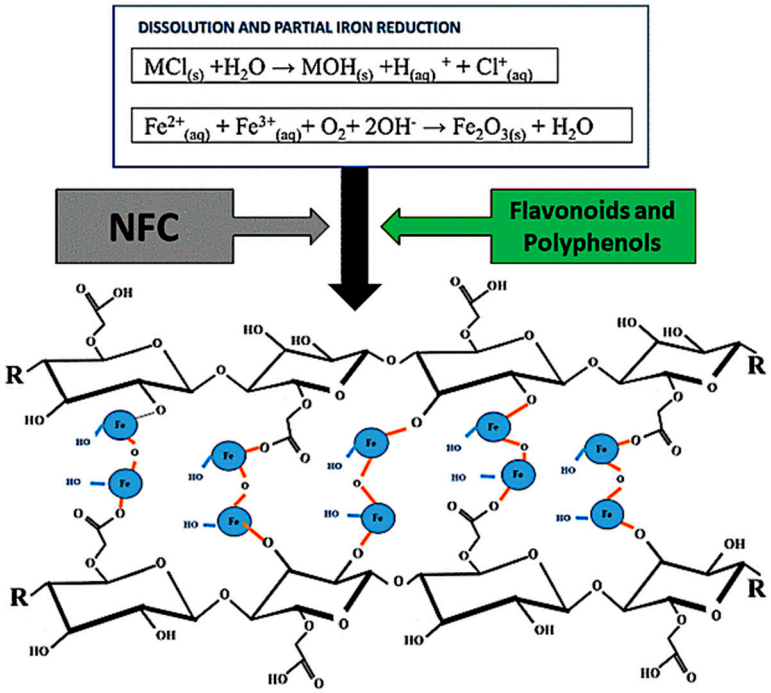

Figure 13. Schematic diagram of iron nanoparticle formation.

Cellulose nanofibers (NFCs) contain cellulose, simple sugars, and carbonaceous compounds that can bind to heavy metals. In nanoparticle synthesis, various compounds such as secondary metabolites and phytochemicals (phenolics, flavonoids, and fatty acids) have been introduced; these contribute to the metals' adsorptions. The significant importance of the polymeric matrix support and the nanoparticles' green synthesis processes can be attributed to carbonyl's complexation capacity with the metal ions. Therefore, it is observed that carbonyls are partially converted into carboxylic anions [97]. The FTIR confirmed this conversion in NFC and FeNP/NFC samples where functional groups such as carbonyl (-C=O), carboxylate (-COO), carboxyl (-COOH) in the range from 1000 to 1640 cm^{-1} are shown. These functional groups contribute to the adsorption mechanisms in the CdRM and PbRM samples of the FTIR spectra. They showed a significant reduction in the 1270, 1268, and 1610 cm^{-1} peaks of the carboxyl group (-COOH). Other groups also participated, such as the sulfonic group (-SO) with a band at 1059 cm^{-1}, iron hydroxide group (-FeOH) at 1023 cm^{-1}, and iron oxide group (-FeO) at 601 cm^{-1}.

The overall mechanism is a solid–liquid interfacial reaction, where Cd^{2+} and Pb^{2+} are represented as the metal ions (M^{2+}), Figure 14:

The mechanism for removing Pb^{2+} and Cd^{2+} ions was adsorption onto metallic oxides and nonmetallic sites through ion exchange, electrostatic bonds, and hydrogen bridge bonds. Some oxides (MgO, SiO_2, SO_3, Fe_2O_3) cause ligand chelation due to oxygen in the range from 4.5 to 5 pH used in these experiments (Figure 14b). The negative charge of the adsorbent, independently of the solution's pH, helps in the adsorption of these ions. These factors contribute to the formation of internal and external complexes by the various hydroxyl (-OH) groups present in the material, as shown in Figure 14c,d [56]. Electrostatic interactions would only occur with the weakest bound cations (Figure 14a). Hydroxyl (-OH) groups close to carboxyl (-COOH) groups would participate in the complexation of the highly bound cations and allow at least two functional carboxyl groups to contain a divalent cation.

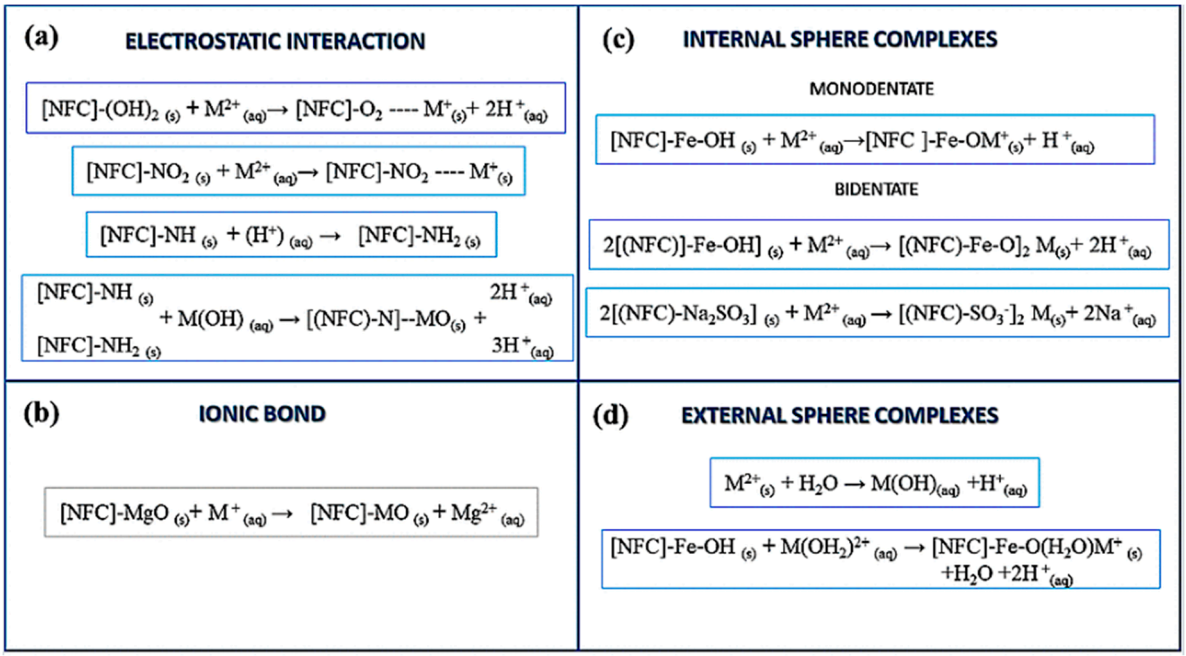

Figure 14. Metal ion (M^{2+}) adsorption mechanisms on composite adsorbent: (**a**) electrostatic interactions, (**b**) ionic bond formation, (**c**) internal sphere complexes formation, (**d**) external sphere complexes formation. [3,56,85,102,103].

The inner-sphere complex is formed by a covalent bond between the oxide's oxygen on the adsorbent's surface (-FeO) or the polymer's oxygen with the metal ion (M^{2+}). These possible mechanisms cause the loss of protons to the solutions, reducing the pH. Monodentate and bidentate complexes are formed depending on the presence of hydroxyl groups (Figure 15). The outer-sphere complex is formed when water is present between the adsorbed metal ion and the hydroxyl group on the iron (Fe-OH) surface. This complex can be distinguished because the bond is weaker than the inner-sphere complexes that form an electrostatic bond between the metal ions and the functional groups on the surface [3].

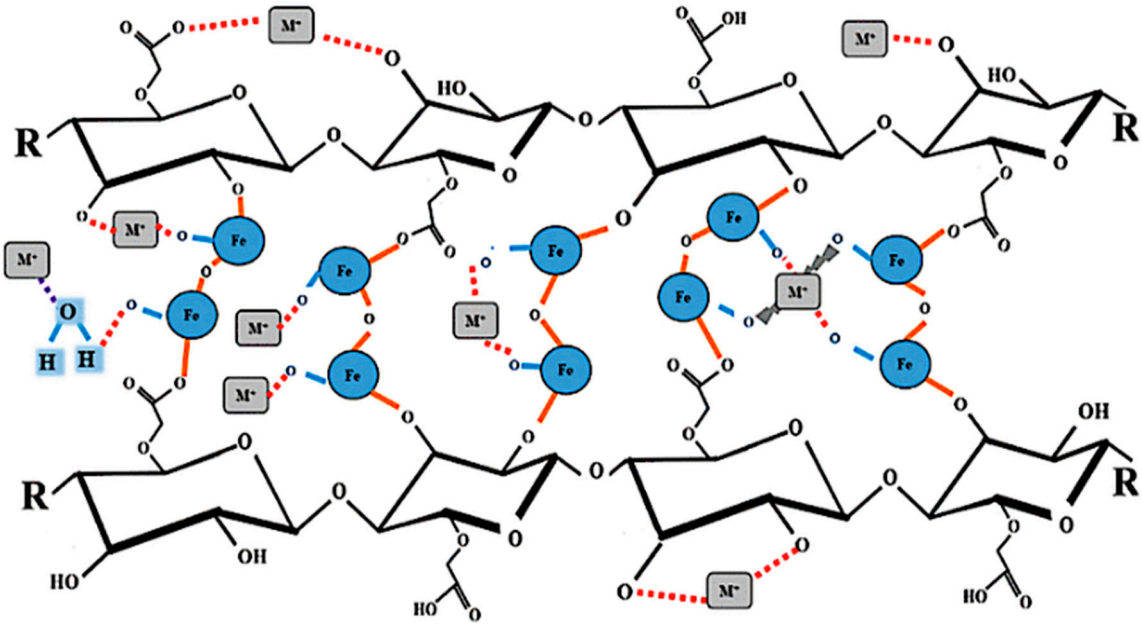

Figure 15. Scheme of adsorption mechanisms on FeNP/NFC.

The Kraft pulping and acid hydrolysis processes formed the anionic sulfonated cellulose derivatives, where the oxidation of the cellulose and sulfonation with the reagents used in these processes occurs. Material modifications, such as mercerization or sulfurization, increase the adsorption capacity of lignocellulosic materials. Sulfonated nanocelluloses have a large number of binding sites due to the different surfaces observed in the material. The participation in the adsorption of the sulfonic groups was important, as well as the carboxyl or hydroxyl groups. Sulfur forms complexes with ligands with a more covalent character instead of ionic, where metal ions (M^{2+}) bind with two oxygenates to form complexes, as illustrated in Figure 16a:

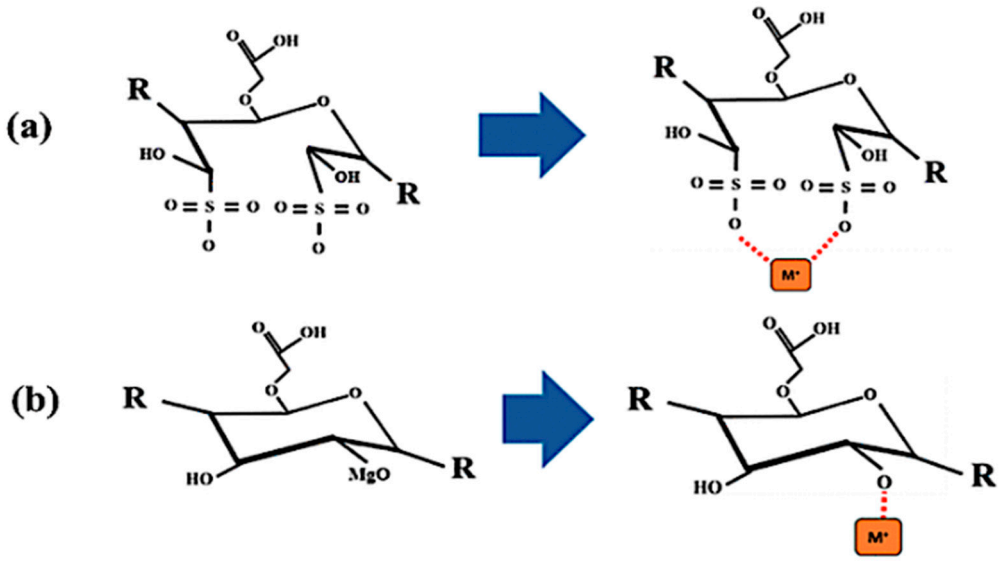

Figure 16. Adsorption mechanism on FeNP/NFC: (**a**) sulfur forms complexes and (**b**) ionic bonds.

The exchange of metal ions (M^2) with H^+ ions of hydroxyl groups on the surface occurs because the cations in the aqueous solutions are hydrated; therefore, they are attracted to the surface's functional group of interest. Mg^{2+} can participate in the adsorption. This result indicates that the magnesium ions, which were part of the MgO crystals in the FeNP/NFC composite, exchange with the M^{2+} during adsorption—Figure 16b [67]. As with many other adsorbent materials, there is the possibility that two or more mechanisms are involved in adsorption, as there are several active groups in FeNP/NFC.

The amino group on NFC, as mentioned above, influences the mechanism of lead removal. Metal ions can interact and bind with two binding sites on the surface [104]. There seems to be a significant impact on the ionization ability of –NH by pH, which affects the adsorption capacity of target ions. H^+ concentration is high in solution when pH is low; thus, –NH of material is protonated in this environment. This behavior will enhance the electrostatic attraction of anions, further increasing target ions' adsorption capacity [105].

4. Conclusions

Having Fe nanoparticles on the FeNP/NFC composite improved Cd and Pb selectivity during removal processes. The various chemical reaction processes (carboxymethylation, oxidation, hydrolysis, and sulfonation) occurred during the Kraft process, and acid hydrolysis increased the composite's heterogeneous surface. The chemical structure of the FeNP/NFC surface (adsorption sites and hydroxyl coordination) depends on the oxides' morphologies and the crystal structure. The high content of minerals or inorganic substances does not interfere with the adsorption process; otherwise, they helped to functionalize the material and diversify the adsorption mechanisms. Cd and Pb ions' speciation in an aqueous solution at pH 5 affects and determines the charge that will allow adsorption. As seen in the zeta potential results, the composite is negatively charged, so cations were

easily adsorbed. Cd and Pb sorption mechanisms are related to electrostatic interactions, hydrogen bonding, and ion exchange with biopolymer structures. The strong electrostatic interactions between the -OH ions and the carboxyl groups were essential to form inner-sphere and outer-sphere complexes in the material. The thermodynamic results indicate that both processes have exothermic reactions which are irreversible and stable. The pseudo-first-order model describes Pb sorption kinetics well. Still, the Elovich equation was also a good model to describe Cd sorption kinetics. Based on the adsorption capacities obtained in this study, FeNP/NFC can be considered as a highly efficient adsorbent to remove these ions from aqueous solutions, particularly for Pb.

Author Contributions: Conceptualization, A.V.-G., R.C.-M., and R.H.-A.; methodology, A.V.-G. and R.C.-M.; software, A.V.-G.; validation, A.V.-G, R.A.-C.-V., and R.H.-A.; formal analysis, E.M.R.-M. and R.H.-A; investigation, A.V.-G. and E.M.R.-M.; resources, R.A.-C.-V., R.H.-A. and R.C.-M.; data curation, A.V.-G. and E.M.R.-M.; writing—original draft preparation, A.V.-G.; writing—review and editing, R.C.-M., R.H.-A., and R.A.-C.-V.; supervision, R.C.-M., R.H.-A., and R.A.-C.-V.; funding acquisition, R.A.-C.-V. All authors have read and agreed to the published version of the manuscript.

Funding: This research was funded by Coordinación de la Investigación Científica-UMSNH, grant number CIC-UMSNH-2020, and the APC was funded by PRODEP.

Institutional Review Board Statement: Not applicable.

Informed Consent Statement: Not applicable.

Acknowledgments: We appreciate the technical support provided by B. Millán-Malo from CFATA-UNAM.

Conflicts of Interest: The authors declare no conflict of interest. The funders had no role in the design of the study; in the collection, analyses, or interpretation of data; in the writing of the manuscript, or in the decision to publish the results.

References

1. Riani, E.; Cordova, M.R.; Arifin, Z. Heavy Metal Pollution and Its Relation to the Malformation of Green Mussels Cultured in Muara Kamal Waters, Jakarta Bay, Indonesia. *Mar. Pollut. Bull.* **2018**, *133*, 664–670. [CrossRef] [PubMed]
2. Fijałkowska, G.; Szewczuk-Karpisz, K.; Wiśniewska, M. Chromium(VI) and Lead(II) Accumulation at the Montmorillonite/Aqueous Solution Interface in the Presence of Polyacrylamide Containing Quaternary Amine Groups. *J. Mol. Liq.* **2019**, *293*, 111514. [CrossRef]
3. Kumari, M.; Pittman, C.U.; Mohan, D. Heavy Metals [Chromium (VI) and Lead (II)] Removal from Water Using Mesoporous Magnetite (Fe3O4) Nanospheres. *J. Colloid Interface Sci.* **2015**, *442*, 120–132. [CrossRef] [PubMed]
4. Sharma, R.; Sarswat, A.; Pittman, C.U.; Mohan, D. Cadmium and Lead Remediation Using Magnetic and Non-Magnetic Sustainable Biosorbents Derived from Bauhinia Purpurea Pods. *RSC Adv.* **2017**, *7*, 8606–8624. [CrossRef]
5. Koju, N.K.; Song, X.; Wang, Q.; Hu, Z.; Colombo, C. Cadmium Removal from Simulated Groundwater Using Alumina Nanoparticles: Behaviors and Mechanisms. *Environ. Pollut.* **2018**, *240*, 255–266. [CrossRef]
6. Chen, Z.; Zhang, J.; Huang, L.; Yuan, Z.; Li, Z.; Liu, M. Removal of Cd and Pb with Biochar Made from Dairy Manure at Low Temperature. *J. Integr. Agric.* **2019**, *18*, 201–210. [CrossRef]
7. Jaishankar, M.; Tseten, T.; Anbalagan, N.; Mathew, B.B.; Beeregowda, K.N. Toxicity, Mechanism and Health Effects of Some Heavy Metals. *Interdiscip. Toxicol.* **2014**, *7*, 60–72. [CrossRef]
8. Mohan, D.; Pittman, C.U.; Bricka, M.; Smith, F.; Yancey, B.; Mohammad, J.; Steele, P.H.; Alexandre-Franco, M.F.; Gómez-Serrano, V.; Gong, H. Sorption of Arsenic, Cadmium, and Lead by Chars Produced from Fast Pyrolysis of Wood and Bark during Bio-Oil Production. *J. Colloid Interface Sci.* **2007**, *310*, 57–73. [CrossRef]
9. Mager, E.M.; Brix, K.V.; Gerdes, R.M.; Ryan, A.C.; Grosell, M. Effects of Water Chemistry on the Chronic Toxicity of Lead to the Cladoceran, Ceriodaphnia Dubia. *Ecotoxicol. Environ. Saf.* **2011**, *74*, 238–243. [CrossRef]
10. Akinyeye, O.J.; Ibigbami, T.B.; Odeja, O.O.; Sosanolu, O.M. Evaluation of Kinetics and Equilibrium Studies of Biosorption Potentials of Bamboo Stem Biomass for Removal of Lead (II) and Cadmium (II) Ions from Aqueous Solution. *Afr. J. Pure Appl. Chem.* **2020**, *14*, 24–41. [CrossRef]
11. Isawi, H. Using Zeolite/Polyvinyl Alcohol/Sodium Alginate Nanocomposite Beads for Removal of Some Heavy Metals from Wastewater. *Arab. J. Chem.* **2020**, *13*, 5691–5716. [CrossRef]
12. Ahmad, R.; Mirza, A. Facile One Pot Green Synthesis of Chitosan-Iron Oxide (CS-Fe2O3) Nanocomposite: Removal of Pb(II) and Cd(II) from Synthetic and Industrial Wastewater. *J. Clean. Prod.* **2018**, *186*, 342–352. [CrossRef]
13. O'Connell, D.W.; Birkinshaw, C.; O'Dwyer, T.F. Heavy Metal Adsorbents Prepared from the Modification of Cellulose: A Review. *Bioresour. Technol.* **2008**, *99*, 6709–6724. [CrossRef] [PubMed]

14. Valdés Rodríguez, O.A.; Palacios Wassenaar, O.M.; Ruíz Hernández, R.; Pérez Vásquez, A. Moringa and Ricinus Association Potential in the Sub-Tropics of Veracruz. *Rev. Mex. Cienc. Agríc.* **2014**, *5*, 1673–1686.
15. Olson, M.E.; Fahey, J.W. Moringa oleifera: Un árbol multiusos para las zonas tropicales secas. *Rev. Mex. Biodivers.* **2011**, *82*, 1071–1082. [CrossRef]
16. Kargarzadeh, H.; Ahmad, I.; Abdullah, I.; Dufresne, A.; Zainudin, S.Y.; Sheltami, R.M. Effects of Hydrolysis Conditions on the Morphology, Crystallinity, and Thermal Stability of Cellulose Nanocrystals Extracted from Kenaf Bast Fibers. *Cellulose* **2012**, *19*, 855–866. [CrossRef]
17. Ramos-Vargas, S.; Huirache-Acuña, R.; Guadalupe Rutiaga-Quiñones, J.; Cortés-Martínez, R. Effective Lead Removal from Aqueous Solutions Using Cellulose Nanofibers Obtained from Water Hyacinth. *Water Supply* **2020**, *20*, 2715–2736. [CrossRef]
18. Mahfoudhi, N.; Boufi, S. Nanocellulose as a Novel Nanostructured Adsorbent for Environmental Remediation: A Review. *Cellulose* **2017**, *24*, 1171–1197. [CrossRef]
19. Rahmani, A.; Mousavi, H.Z.; Fazli, M. Effect of Nanostructure Alumina on Adsorption of Heavy Metals. *Desalination* **2010**, *253*, 94–100. [CrossRef]
20. Mondal, P.; Purkait, M.K. Green Synthesized Iron Nanoparticles Supported on PH Responsive Polymeric Membrane for Nitrobenzene Reduction and Fluoride Rejection Study: Optimization Approach. *J. Clean. Prod.* **2018**, *170*, 1111–1123. [CrossRef]
21. Bolade, O.P.; Williams, A.B.; Benson, N.U. Green Synthesis of Iron-Based Nanomaterials for Environmental Remediation: A Review. *Environ. Nanotechnol. Monit. Manag.* **2020**, *13*, 100279. [CrossRef]
22. Abujaber, F.; Zougagh, M.; Jodeh, S.; Ríos, Á.; Guzmán Bernardo, F.J.; Rodríguez Martín-Doimeadios, R.C. Magnetic Cellulose Nanoparticles Coated with Ionic Liquid as a New Material for the Simple and Fast Monitoring of Emerging Pollutants in Waters by Magnetic Solid Phase Extraction. *Microchem. J.* **2018**, *137*, 490–495. [CrossRef]
23. Krishna, R.; Dias, C.; Ventura, J.; Titus, E. Green and Facile Decoration of Fe3O4 Nanoparticles on Reduced Graphene Oxide. *Mater. Today Proc.* **2016**, *3*, 2807–2813. [CrossRef]
24. Ostovan, A.; Ghaedi, M.; Arabi, M. Fabrication of Water-Compatible Superparamagnetic Molecularly Imprinted Biopolymer for Clean Separation of Baclofen from Bio-Fluid Samples: A Mild and Green Approach. *Talanta* **2018**, *179*, 760–768. [CrossRef]
25. Soliemanzadeh, A.; Fekri, M. The Application of Green Tea Extract to Prepare Bentonite-Supported Nanoscale Zero-Valent Iron and Its Performance on Removal of Cr(VI): Effect of Relative Parameters and Soil Experiments. *Microporous Mesoporous Mater.* **2017**, *239*, 60–69. [CrossRef]
26. Wang, X.; Le, L.; Alvarez, P.J.J.; Li, F.; Liu, K. Synthesis and Characterization of Green Agents Coated Pd/Fe Bimetallic Nanoparticles. *J. Taiwan Inst. Chem. Eng.* **2015**, *50*, 297–305. [CrossRef]
27. Zhang, Y.; Chen, Y.; Westerhoff, P.; Hristovski, K.; Crittenden, J.C. Stability of Commercial Metal Oxide Nanoparticles in Water. *Water Res.* **2008**, *42*, 2204–2212. [CrossRef]
28. Liu, L.; Fan, S. Removal of Cadmium in Aqueous Solution Using Wheat Straw Biochar: Effect of Minerals and Mechanism. *Environ. Sci. Pollut. Res.* **2018**, *25*, 8688–8700. [CrossRef]
29. Bibi, I.; Nazar, N.; Ata, S.; Sultan, M.; Ali, A.; Abbas, A.; Jilani, K.; Kamal, S.; Sarim, F.M.; Khan, M.I.; et al. Green Synthesis of Iron Oxide Nanoparticles Using Pomegranate Seeds Extract and Photocatalytic Activity Evaluation for the Degradation of Textile Dye. *J. Mater. Res. Technol.* **2019**, *8*, 6115–6124. [CrossRef]
30. Bolade, O.P.; Akinsiku, A.A.; Adeyemi, A.O.; Williams, A.B.; Benson, N.U. Dataset on Phytochemical Screening, FTIR and GC–MS Characterisation of Azadirachta Indica and Cymbopogon Citratus as Reducing and Stabilising Agents for Nanoparticles Synthesis. *Data Brief* **2018**, *20*, 917–926. [CrossRef]
31. Akhtar, M.S.; Panwar, J.; Yun, Y.-S. Biogenic Synthesis of Metallic Nanoparticles by Plant Extracts. *ACS Sustain. Chem. Eng.* **2013**, *1*, 591–602. [CrossRef]
32. Kharissova, O.V.; Dias, H.V.R.; Kharisov, B.I.; Pérez, B.O.; Pérez, V.M.J. The Greener Synthesis of Nanoparticles. *Trends Biotechnol.* **2013**, *31*, 240–248. [CrossRef] [PubMed]
33. Nasrollahzadeh, M.; Mohammad Sajadi, S.; Rostami-Vartooni, A.; Khalaj, M. Green Synthesis of Pd/Fe3O4 Nanoparticles Using Euphorbia Condylocarpa M. Bieb Root Extract and Their Catalytic Applications as Magnetically Recoverable and Stable Recyclable Catalysts for the Phosphine-Free Sonogashira and Suzuki Coupling Reactions. *J. Mol. Catal. Chem.* **2015**, *396*, 31–39. [CrossRef]
34. Harshiny, M.; Iswarya, C.N.; Matheswaran, M. Biogenic Synthesis of Iron Nanoparticles Using Amaranthus Dubius Leaf Extract as a Reducing Agent. *Powder Technol.* **2015**, *286*, 744–749. [CrossRef]
35. Cai, Y.; Shen, Y.; Xie, A.; Li, S.; Wang, X. Green Synthesis of Soya Bean Sprouts-Mediated Superparamagnetic Fe3O4 Nanoparticles. *J. Magn. Magn. Mater.* **2010**, *322*, 2938–2943. [CrossRef]
36. Makarov, V.V.; Makarova, S.S.; Love, A.J.; Sinitsyna, O.V.; Dudnik, A.O.; Yaminsky, I.V.; Taliansky, M.E.; Kalinina, N.O. Biosynthesis of Stable Iron Oxide Nanoparticles in Aqueous Extracts of Hordeum Vulgare and Rumex Acetosa Plants. *Langmuir* **2014**, *30*, 5982–5988. [CrossRef]
37. Balamurugan, M.; Saravanan, S.; Soga, T. Synthesis of Iron Oxide Nanoparticles by Using *Eucalyptus Globulus* Plant Extract. *E-J. Surf. Sci. Nanotechnol.* **2014**, *12*, 363–367. [CrossRef]
38. Harshiny, M.; Matheswaran, M.; Arthanareeswaran, G.; Kumaran, S.; Rajasree, S. Enhancement of Antibacterial Properties of Silver Nanoparticles–Ceftriaxone Conjugate through Mukia Maderaspatana Leaf Extract Mediated Synthesis. *Ecotoxicol. Environ. Saf.* **2015**, *121*, 135–141. [CrossRef]

39. Ahmmad, B.; Leonard, K.; Shariful Islam, M.; Kurawaki, J.; Muruganandham, M.; Ohkubo, T.; Kuroda, Y. Green Synthesis of Mesoporous Hematite (α-Fe2O3) Nanoparticles and Their Photocatalytic Activity. *Adv. Powder Technol.* **2013**, *24*, 160–167. [CrossRef]
40. Wang, Z.; Fang, C.; Megharaj, M. Characterization of Iron–Polyphenol Nanoparticles Synthesized by Three Plant Extracts and Their Fenton Oxidation of Azo Dye. *ACS Sustain. Chem. Eng.* **2014**, *2*, 1022–1025. [CrossRef]
41. Li, J.; Hu, J.; Xiao, L.; Wang, Y.; Wang, X. Interaction Mechanisms between α-Fe2O3, γ-Fe2O3 and Fe3O4 Nanoparticles and Citrus Maxima Seedlings. *Sci. Total Environ.* **2018**, *625*, 677–685. [CrossRef] [PubMed]
42. Devatha, C.P.; K, J.; Patil, M. Effect of Green Synthesized Iron Nanoparticles by Azardirachta Indica in Different Proportions on Antibacterial Activity. *Environ. Nanotechnol. Monit. Manag.* **2018**, *9*, 85–94. [CrossRef]
43. Zhu, F.; Ma, S.; Liu, T.; Deng, X. Green Synthesis of Nano Zero-Valent Iron/Cu by Green Tea to Remove Hexavalent Chromium from Groundwater. *J. Clean. Prod.* **2018**, *174*, 184–190. [CrossRef]
44. Weng, X.; Guo, M.; Luo, F.; Chen, Z. One-Step Green Synthesis of Bimetallic Fe/Ni Nanoparticles by Eucalyptus Leaf Extract: Biomolecules Identification, Characterization and Catalytic Activity. *Chem. Eng. J.* **2017**, *308*, 904–911. [CrossRef]
45. Abdelghany, T.M.; Al-Rajhi, A.M.H.; Al Abboud, M.A.; Alawlaqi, M.M.; Ganash Magdah, A.; Helmy, E.A.M.; Mabrouk, A.S. Recent Advances in Green Synthesis of Silver Nanoparticles and Their Applications: About Future Directions. A Review. *BioNanoScience* **2018**, *8*, 5–16. [CrossRef]
46. Ahmed, S.; Ahmad, M.; Swami, B.L.; Ikram, S. A Review on Plants Extract Mediated Synthesis of Silver Nanoparticles for Antimicrobial Applications: A Green Expertise. *J. Adv. Res.* **2016**, *7*, 17–28. [CrossRef] [PubMed]
47. Iqbal, A.; Iqbal, K.; Li, B.; Gong, D.; Qin, W. Recent Advances in Iron Nanoparticles: Preparation, Properties, Biological and Environmental Application. *J. Nanosci. Nanotechnol.* **2017**, *17*, 4386–4409. [CrossRef]
48. Saif, S.; Tahir, A.; Chen, Y. Green Synthesis of Iron Nanoparticles and Their Environmental Applications and Implications. *Nanomaterials* **2016**, *6*, 209. [CrossRef]
49. Rauwel, P.; Küünal, S.; Ferdov, S.; Rauwel, E. A Review on the Green Synthesis of Silver Nanoparticles and Their Morphologies Studied via TEM. Available online: https://www.hindawi.com/journals/amse/2015/682749/ (accessed on 4 October 2020).
50. Sharma, J.K.; Srivastava, P.; Akhtar, M.S.; Singh, G.; Ameen, S. α-Fe2O3 Hexagonal Cones Synthesized from the Leaf Extract of Azadirachta Indica and Its Thermal Catalytic Activity. *New J. Chem.* **2015**, *39*, 7105–7111. [CrossRef]
51. Falowo, A.B.; Mukumbo, F.E.; Idamokoro, E.M.; Lorenzo, J.M.; Afolayan, A.J.; Muchenje, V. Multi-Functional Application of Moringa Oleifera Lam. in Nutrition and Animal Food Products: A Review. *Food Res. Int.* **2018**, *106*, 317–334. [CrossRef]
52. Waterman, C.; Cheng, D.M.; Rojas-Silva, P.; Poulev, A.; Dreifus, J.; Lila, M.A.; Raskin, I. Stable, Water Extractable Isothiocyanates from Moringa Oleifera Leaves Attenuate Inflammation in Vitro. *Phytochemistry* **2014**, *103*, 114–122. [CrossRef] [PubMed]
53. Lagergren, S. Zur theorie der sogenannten adsorption geloster stoffe. Kungliga Svenska Vetenskapsakademiens. *Handlingar* **1898**, *24*, 1–39.
54. Ho, Y.S.; McKay, G.; Wase, D.A.J.; Forster, C.F. Study of the Sorption of Divalent Metal Ions on to Peat. *Adsorpt. Sci. Technol.* **2000**, *18*, 639–650. [CrossRef]
55. Low, M.J.D. Kinetics of Chemisorption of Gases on Solids. Available online: https://pubs.acs.org/doi/pdf/10.1021/cr60205a003 (accessed on 3 October 2020).
56. Chen, K.; He, J.; Li, Y.; Cai, X.; Zhang, K.; Liu, T.; Hu, Y.; Lin, D.; Kong, L.; Liu, J. Removal of Cadmium and Lead Ions from Water by Sulfonated Magnetic Nanoparticle Adsorbents. *J. Colloid Interface Sci.* **2017**, *494*, 307–316. [CrossRef] [PubMed]
57. Langmuir, I. The Adsorption of Gases on Plane Surfaces of Glass, Mica and Platinum. *J. Am. Chem. Soc.* **1918**, *40*, 1361–1403. [CrossRef]
58. Papageorgiou, S.K.; Kouvelos, E.P.; Katsaros, F.K. Calcium Alginate Beads from Laminaria Digitata for the Removal of Cu^{+2} and Cd^{+2} from Dilute Aqueous Metal Solutions. *Desalination* **2008**, *224*, 293–306. [CrossRef]
59. Acemioğlu, B. Removal of Fe(II) Ions from Aqueous Solution by Calabrian Pine Bark Wastes. *Bioresour. Technol.* **2004**, *93*, 99–102. [CrossRef]
60. Sivarathnakumar, S.; Baskar, G.; Kumar, R.P.; Bharathiraja, B. Bioethanol Production by the Utilisation of Moringa Oleifera Stem with Sono-Assisted Acid/Alkali Hydrolysis Approach. *Int. J. Environ. Sustain. Dev.* **2016**, *15*, 392–403. [CrossRef]
61. Zhao, H.; Kwak, J.H.; Conrad Zhang, Z.; Brown, H.M.; Arey, B.W.; Holladay, J.E. Studying Cellulose Fiber Structure by SEM, XRD, NMR and Acid Hydrolysis. *Carbohydr. Polym.* **2007**, *68*, 235–241. [CrossRef]
62. Lavoine, N.; Desloges, I.; Dufresne, A.; Bras, J. Microfibrillated Cellulose—Its Barrier Properties and Applications in Cellulosic Materials: A Review. *Carbohydr. Polym.* **2012**, *90*, 735–764. [CrossRef]
63. Kumar, A.; Negi, Y.S.; Choudhary, V.; Bhardwaj, N.K. Characterization of Cellulose Nanocrystals Produced by Acid-Hydrolysis from Sugarcane Bagasse as Agro-Waste. *J. Mater. Phys. Chem.* **2014**, *2*, 1–8. [CrossRef]
64. Zhao, Y.; Xu, C.; Xing, C.; Shi, X.; Matuana, L.M.; Zhou, H.; Ma, X. Fabrication and Characteristics of Cellulose Nanofibril Films from Coconut Palm Petiole Prepared by Different Mechanical Processing. *Ind. Crops Prod.* **2015**, *65*, 96–101. [CrossRef]
65. Abdul Khalil, H.P.S.; Davoudpour, Y.; Islam, M.N.; Mustapha, A.; Sudesh, K.; Dungani, R.; Jawaid, M. Production and Modification of Nanofibrillated Cellulose Using Various Mechanical Processes: A Review. *Carbohydr. Polym.* **2014**, *99*, 649–665. [CrossRef] [PubMed]

66. Tonoli, G.H.D.; Teixeira, E.M.; Corrêa, A.C.; Marconcini, J.M.; Caixeta, L.A.; Pereira-da-Silva, M.A.; Mattoso, L.H.C. Cellulose Micro/Nanofibres from Eucalyptus Kraft Pulp: Preparation and Properties. *Carbohydr. Polym.* **2012**, *89*, 80–88. [CrossRef] [PubMed]
67. Kalia, S.; Dufresne, A.; Cherian, B.M.; Kaith, B.S.; Avérous, L.; Njuguna, J.; Nassiopoulos, E. Cellulose-Based Bio- and Nanocomposites: A Review. Available online: https://www.hindawi.com/journals/ijps/2011/837875/ (accessed on 27 December 2020).
68. Dong, H.; Snyder, J.F.; Tran, D.T.; Leadore, J.L. Hydrogel, Aerogel and Film of Cellulose Nanofibrils Functionalized with Silver Nanoparticles. *Carbohydr. Polym.* **2013**, *95*, 760–767. [CrossRef]
69. Sahu, U.K.; Mahapatra, S.S.; Patel, R.K. Synthesis and Characterization of an Eco-Friendly Composite of Jute Fiber and Fe_2O_3 Nanoparticles and Its Application as an Adsorbent for Removal of As(V) from Water. *J. Mol. Liq.* **2017**, *237*, 313–321. [CrossRef]
70. Nagappan, S.; Ha, H.M.; Park, S.S.; Jo, N.-J.; Ha, C.-S. One-Pot Synthesis of Multi-Functional Magnetite–Polysilsesquioxane Hybrid Nanoparticles for the Selective Fe^{3+} and Some Heavy Metal Ions Adsorption. *RSC Adv.* **2017**, *7*, 19106–19116. [CrossRef]
71. Cao, C.-Y.; Qu, J.; Wei, F.; Liu, H.; Song, W.-G. Superb Adsorption Capacity and Mechanism of Flowerlike Magnesium Oxide Nanostructures for Lead and Cadmium Ions. *ACS Appl. Mater. Interfaces* **2012**, *4*, 4283–4287. [CrossRef]
72. Xu, Q.; Jiang, L. Infrared Spectra of the M(NO)n (M = Sn, Pb; n = 1, 2) and PbNO- Molecules. *Inorg. Chem.* **2006**, *45*, 8648–8654. [CrossRef]
73. Qin, X.; Zhou, J.; Huang, A.; Guan, J.; Zhang, Q.; Huang, Z.; Hu, H.; Zhang, Y.; Yang, M.; Wu, J.; et al. A Green Technology for the Synthesis of Cellulose Succinate for Efficient Adsorption of Cd(II) and Pb(II) Ions. *RSC Adv.* **2016**, *6*, 26817–26825. [CrossRef]
74. Asmaly, H.A.; Abussaud, B.; Ihsanullah; Saleh, T.A.; Bukhari, A.A.; Laoui, T.; Shemsi, A.M.; Gupta, V.K.; Atieh, M.A. Evaluation of Micro- and Nano-Carbon-Based Adsorbents for the Removal of Phenol from Aqueous Solutions. *Toxicol. Environ. Chem.* **2015**, *97*, 1164–1179. [CrossRef]
75. Taipale, T.; Österberg, M.; Nykänen, A.; Ruokolainen, J.; Laine, J. Effect of Microfibrillated Cellulose and Fines on the Drainage of Kraft Pulp Suspension and Paper Strength. *Cellulose* **2010**, *17*, 1005–1020. [CrossRef]
76. Capron, I.; Rojas, O.J.; Bordes, R. Behavior of Nanocelluloses at Interfaces. *Curr. Opin. Colloid Interface Sci.* **2017**, *29*, 83–95. [CrossRef]
77. Visakh, P.M.; Mathew, A.P.; Oksman, K.; Thomas, S. Starch-Based Bionanocomposites: Processing and Properties. In *Polysaccharide Building Blocks*; John Wiley & Sons, Ltd.: Hoboken, NJ, USA, 2012; pp. 287–306. ISBN 978-1-118-22948-4.
78. Fengel, D.; Wegener, G. *Wood: Chemistry, Ultrastructure, Reactions*; Walter de Gruyter: Berlin, Germany, 2011; ISBN 978-3-11-083965-4.
79. Martínez-Pérez, R.; Pedraza-Bucio, F.E.; Orihuela-Equihua, R.; López-Albarrán, P.; Rutiaga-Quiñones, J.G. Calorific Value and Inorganic Material of Ten Mexican Wood Species. *Wood Res.* **2015**, *60*, 12.
80. Argyropoulos, D.S. Wood and Cellulosic Chemistry. Second Edition, Revised and Expanded Edited by David N.-S. Hon (Clemson University) and Nubuo Shiraishi (Kyoto University). Marcel Dekker: New York and Basel. 2001. Vii + 914 Pp. $250.00. ISBN 0-8247-0024-4. *J. Am. Chem. Soc.* **2001**, *123*, 8880–8881. [CrossRef]
81. Ngangyo-Heya, M.; Foroughbahchk-Pournavab, R.; Carrillo-Parra, A.; Rutiaga-Quiñones, J.G.; Zelinski, V.; Pintor-Ibarra, L.F. Calorific Value and Chemical Composition of Five Semi-Arid Mexican Tree Species. *Forests* **2016**, *7*, 58. [CrossRef]
82. Muthukumar, H.; Matheswaran, M. Amaranthus Spinosus Leaf Extract Mediated FeO Nanoparticles: Physicochemical Traits, Photocatalytic and Antioxidant Activity. *ACS Sustain. Chem. Eng.* **2015**, *3*, 3149–3156. [CrossRef]
83. Zhu, X.; Song, T.; Lv, Z.; Ji, G. High-Efficiency and Low-Cost α-Fe2O3 Nanoparticles-Coated Volcanic Rock for Cd(II) Removal from Wastewater. *Process Saf. Environ. Prot.* **2016**, *104*, 373–381. [CrossRef]
84. Tajik, E.; Naeimi, A.; Amiri, A. Fabrication of Iron Oxide Nanoparticles, and Green Catalytic Application of an Immobilized Novel Iron Schiff on Wood Cellulose. *Cellulose* **2018**, *25*, 915–923. [CrossRef]
85. Gupta, V.K.; Nayak, A. Cadmium Removal and Recovery from Aqueous Solutions by Novel Adsorbents Prepared from Orange Peel and Fe2O3 Nanoparticles. *Chem. Eng. J.* **2012**, *180*, 81–90. [CrossRef]
86. Foo, K.Y.; Hameed, B.H. Insights into the Modeling of Adsorption Isotherm Systems. *Chem. Eng. J.* **2010**, *156*, 2–10. [CrossRef]
87. Papageorgiou, S.K.; Katsaros, F.K.; Kouvelos, E.P.; Nolan, J.W.; Le Deit, H.; Kanellopoulos, N.K. Heavy Metal Sorption by Calcium Alginate Beads from Laminaria Digitata. *J. Hazard. Mater.* **2006**, *137*, 1765–1772. [CrossRef] [PubMed]
88. Wang, F.; Lu, X.; Li, X. Selective Removals of Heavy Metals (Pb2+, Cu2+, and Cd2+) from Wastewater by Gelation with Alginate for Effective Metal Recovery. *J. Hazard. Mater.* **2016**, *308*, 75–83. [CrossRef] [PubMed]
89. Pawar, R.R.; Lalhmunsiama; Kim, M.; Kim, J.-G.; Hong, S.-M.; Sawant, S.Y.; Lee, S.M. Efficient Removal of Hazardous Lead, Cadmium, and Arsenic from Aqueous Environment by Iron Oxide Modified Clay-Activated Carbon Composite Beads. *Appl. Clay Sci.* **2018**, *162*, 339–350. [CrossRef]
90. Elimelech, M.; Chen, W.H.; Waypa, J.J. Measuring the Zeta (Electrokinetic) Potential of Reverse Osmosis Membranes by a Streaming Potential Analyzer. *Desalination* **1994**, *95*, 269–286. [CrossRef]
91. Zirino, A.; Yamamoto, S. A pH-Dependent Model for The Chemical Speciation of Copper, Zinc, Cadmium, and Lead in Seawater. *Limnol. Oceanogr.* **1972**, *17*, 661–671. [CrossRef]
92. Giles, C.H.; D'Silva, A.P.; Easton, I.A. A General Treatment and Classification of the Solute Adsorption Isotherm Part. II. Experimental Interpretation. *J. Colloid Interface Sci.* **1974**, *47*, 766–778. [CrossRef]
93. Giles, C.H.; Smith, D.; Huitson, A. A General Treatment and Classification of the Solute Adsorption Isotherm. I. Theoretical. *J. Colloid Interface Sci.* **1974**, *47*, 755–765. [CrossRef]

94. Prasher, S.O.; Beaugeard, M.; Hawari, J.; Bera, P.; Patel, R.M.; Kim, S.H. Biosorption of Heavy Metals by Red Algae (Palmaria Palmata). *Environ. Technol.* **2004**, *25*, 1097–1106. [CrossRef]
95. Trakal, L.; Veselská, V.; Šafařík, I.; Vítková, M.; Číhalová, S.; Komárek, M. Lead and Cadmium Sorption Mechanisms on Magnetically Modified Biochars. *Bioresour. Technol.* **2016**, *203*, 318–324. [CrossRef]
96. Anwar, J.; Shafique, U.; Waheed-uz-Zaman; Salman, M.; Dar, A.; Anwar, S. Removal of Pb(II) and Cd(II) from Water by Adsorption on Peels of Banana. *Bioresour. Technol.* **2010**, *101*, 1752–1755. [CrossRef] [PubMed]
97. Ge, F.; Li, M.-M.; Ye, H.; Zhao, B.-X. Effective Removal of Heavy Metal Ions Cd2+, Zn2+, Pb2+, Cu2+ from Aqueous Solution by Polymer-Modified Magnetic Nanoparticles. *J. Hazard. Mater.* **2012**, *211–212*, 366–372. [CrossRef] [PubMed]
98. Keshvardoostchokami, M.; Babaei, L.; Zamani, A.A.; Parizanganeh, A.H.; Piri, F. Synthesized chitosan/iron oxide nanocomposite and shrimp shell in removal of nickel, cadmium and lead from aqueous solution. *Global J. Environ. Sci. Manag.* **2017**, *3*, 267–278.
99. Pehlivan, E.; Yanık, B.H.; Ahmetli, G.; Pehlivan, M. Equilibrium Isotherm Studies for the Uptake of Cadmium and Lead Ions onto Sugar Beet Pulp. *Bioresour. Technol.* **2008**, *99*, 3520–3527. [CrossRef] [PubMed]
100. Kataria, N.; Garg, V.K. Green Synthesis of Fe3O4 Nanoparticles Loaded Sawdust Carbon for Cadmium (II) Removal from Water: Regeneration and Mechanism. *Chemosphere* **2018**, *208*, 818–828. [CrossRef]
101. Shalaby, T.I.; El-Kady, M.F.; Zaki, A.E.H.M.; El-Kholy, S.M. Preparation and Application of Magnetite Nanoparticles Immobilized on Cellulose Acetate Nanofibers for Lead Removal from Polluted Water. *Water Supply* **2017**, *17*, 176–187. [CrossRef]
102. Mahdavi, M.; Namvar, F.; Ahmad, M.B.; Mohamad, R. Green Biosynthesis and Characterization of Magnetic Iron Oxide (Fe3O4) Nanoparticles Using Seaweed (Sargassum Muticum) Aqueous Extract. *Molecules* **2013**, *18*, 5954–5964. [CrossRef]
103. Gao, S.; Shi, Y.; Zhang, S.; Jiang, K.; Yang, S.; Li, Z.; Takayama-Muromachi, E. Biopolymer-Assisted Green Synthesis of Iron Oxide Nanoparticles and Their Magnetic Properties. *J. Phys. Chem. C* **2008**, *112*, 10398–10401. [CrossRef]
104. Hokkanen, S.; Repo, E.; Suopajärvi, T.; Liimatainen, H.; Niinimaa, J.; Sillanpää, M. Adsorption of Ni(II), Cu(II) and Cd(II) from Aqueous Solutions by Amino Modified Nanostructured Microfibrillated Cellulose. *Cellulose* **2014**, *21*, 1471–1487. [CrossRef]
105. Zhao, T.; Feng, T. Application of Modified Chitosan Microspheres for Nitrate and Phosphate Adsorption from Aqueous Solution. *RSC Adv.* **2016**, *6*, 90878–90886. [CrossRef]